North Atlantic multidecadal variability enhancing decadal extratropical extremes in boreal late summer in the early 21st century

Jie Zhang*, Zhiheng Chen, Haishan Chen, Qianrong Ma, Asaminew Teshome

Key Laboratory of Meteorological Disaster, Ministry of Education (KLME) /Joint International Research Laboratory of Climate and Environment Change (ILCEC)/ Collaborative Innovation Center on Forecast and Evaluation of Meteorological Disasters (CIC-FEMD), Nanjing University of Information Science & Technology, Nanjing, 210044, China

Corresponding author: Jie Zhang*, gs-zhangjie@163.com

Early Online Release: This preliminary version has been accepted for publication in *Journal of Climate*, may be fully cited, and has been assigned DOI 10.1175/JCLI-D-19-0536.1. The final typeset copyedited article will replace the EOR at the above DOI when it is published.

Abstract

In the beginning of the 21st century, weather and climate extremes occurred more and more in extratropical summer, linking to the magnified amplitudes of quasi-stationary waves and external forcing. The study analyzes the relations between multidecadal extratropical extremes in boreal late summer and the North Atlantic (NA, 40°W-0°E, 35°N-65°N) multidecadal variability (NAMV) in the mid-high latitude. The results show that multidecadal extratropical extremes link with the intensified NAMV and the related "+-+" zonal mode of sea surface temperature (SST). 1) The SST mode favors the eastward shift of the negative-phase NA oscillation (NNAO), with a latitudinal pattern of cyclone anomalies over western Europe coast and anticyclones over Greenland, NNAO is helpful to baroclinic energy transfer and a longitudinal wavelike pattern. 2) The SST mode and the eddy-driven jet of NNAO is conducive to a southeast extension of the NA jet that closely conjuncts to the Afro Asian jet, thereby enhancing the jet waveguide and barotropic energy transfer for the maintenance of a low-frequency wave. 3) The effect of the intensified NAMV on warming Europe contributes to the longitudinal temperature gradient like 'cooling

Accepted for publication in *Journal of Climate*. DOI10.1175/JCLI-D-19-0536.1.

ocean and warming land' pattern, which enhances the meridional wind and wave amplitude of the low-frequency wave. Based on the causes, the intensified NAMV and the "+-+" SST mode favors the enhancement of the low-frequency wave and quasi-resonant probability, which magnifies the amplitude of the quasi-stationary wave and enhances extratropical extremes on the decadal timescale.

Introduction

Since the beginning of the 21st century, there have been significant increases in extratropical summertime extremes in the Northern Hemisphere (Coumou and Rahmstorf 2012; Huang et al. 2016a; 2017). The extratropical heatwave extremes with serious impacts include summer heatwaves in North America (2011, 2014, and 2016) and European continents (2003, 2019), as well as in Russia and Japan in 2010 (Stott et al. 2004; Hong et al. 2011; Johnson et al. 2018). The extratropical drought/flood extremes with serious impacts occurred in Europe in 2016/2017 (García-Herrera 2019) and in China in 2009/2010, 2012, and 2016 (Zhang et al. 2019). Are these extremes impacted by global warming or internal variability of the earth-atmosphere interaction system? The causes should be discussed separately,

Accepted for publication in *Journal of Climate*. DOI10.1175/JCLI-D-19-0536.1.

because of the increasing risks of economic loss and the damage of ecological environment (Palmer and Räisänen 2002; Zhang et al. 2015; Huang et al. 2016b; 2019), it is critical to explore the extreme mechanism for the prediction, evaluation and disaster prevention.

From the perspective of circulation anomalies, the magnified quasi-stationary waves frequently occur (Petoukhov et al. 2013; Coumou et al. 2014; Petoukhov et al. 2016), along with weakening and northward shifts of the jets and double jet formation for the waveguides (Francis and Vavrus 2011; Coumou et al. 2014; 2015). Furthermore, the jet anomalies of the northern hemisphere, characterized by large variability in jet position, strength, amplitude and width, modulate the extratropical weather extremes (Screen and Simmonds 2014) and act as one of the potential mechanisms of recent extratropical weather extremes. Jet anomalies link to anthropogenic warming, aerosol and natural variability (Baines and Folland 2007; Francis, and Vavrus 2011; Zhang et al. 2015). The westerly jets include the polar jet and subtropical jet, and the subtropical jet section includes the mid-latitude North Atlantic (NA) jet (Trouet et al. 2018), the North Pacific jet (Strong and Davis 2008;

Accepted for publication in *Journal of Climate*. DOI10.1175/JCLI-D-19-0536.1.

Belmecheri et al. 2017) and the Afro Asian jet (Branstator 2002), however, all of them show inconsistent variability at interannual to decadal timescales. Therefore, considering their different impacts, the jet effect on summer extremes should be discussed separately.

The NA jet has been identified to result in extratropical extremes such as heatwaves and droughts in Europe (Trouet et al. 2018), and NA jet variability is often characterized by using circulation indices such as the NA Oscillation (NAO) and the east Atlantic pattern (Woollings and Blackburn 2012). Moreover, extratropical extremes also link to NAO, consisting of a north-south dipole between Greenland and the mid-latitude NA (Sillmann and Croci-Maspoli 2009). Besides, the Atlantic-Eurasian pattern manifests decadal variability and is termed the Eurasian multidecadal teleconnection (Li and Ruan 2018), which is a key component of NAO effect on Asian climate anomaly (Li et al. 2019).

Given that the variability of extratropical extreme exhibits a wide range of timescales, it is an essential step in weather and climate predictions and risk estimation to understand the characteristics and drivers of extreme and related

Accepted for publication in *Journal of Climate*. DOI10.1175/JCLI-D-19-0536.1.

circulation variability. Previous studies show that NAO is closely related to the mid-high-latitude NA sea surface temperature (SST, Shaman et al. 2009; Trouet et al. 2018); Atlantic-Eurasian pattern is pivotal atmospheric bridge between the NA-SST and Eurasian precipitation (Sun et al. 2015). In addition, the NA-SST pattern is closely associated with recent rapid increase of warm extremes in summertime (Johnson et al. 2018). Therefore, the NA-SST pattern is a considerable forcing in modulating extreme variations.

The NA-SST shows remarkable multidecadal variability, (NAMV, Delworth and Mann, 2000), manifested by the SST oscillation of uniform warm and cold patterns, and the dominant mode of NA-SST in the NA Ocean (0°-80°N) is multidecadal oscillation (Schlesinger and Ramankutty 1994; Kerr 2000). There is a consensus that the NAMV is primarily driven by fluctuations in the strength of the Atlantic meridional overturning circulation (AMOC, Black et al. 2014), anthropogenic forcing, internal dynamics and air-sea interaction (Ottera et al. 2010; Chang et al. 2011), although no consensus mechanism of AMOC effect on NAMV (Booth et al. 2012; Clement et al. 2015; Drews and Greatbatch 2016; O'Reilly et al. 2016; Zhang et al.

Accepted for publication in *Journal of Climate*. DOI10.1175/JCLI-D-19-0536.1.

2016; Zhang, 2017). However, AMOC variations are suggested to induce the multidecadal NA-SST because of associated heat transport fluctuations (Goldenberg et al. 2001; O'Reilly et al. 2016). In turn, the multidecadal NA-SST also influences the AMOC, due to meridional advection by northward currents (Delworth et al. 2016; Li et al. 2017). Through dynamic processes, the NAO leads the NA-SST variability by 15-20 years. Besides, atmospheric circulation affects the thermodynamic forcing, heat advection and surface turbulent heat flux anomalies of the NA Ocean (Eden and Jung 2001), thereby modulates the AMOC and the multidecadal NA-SST (Li et al. 2017).

For the perspective of NA-SST effects on the decadal Eurasian climate, NAMV drives the variability in European climate at decadal timescales (Kushnir 1994; Schlesinger and Ramankutty 1994; Delworth and Mann 2000; Knight et al. 2006; 2009; Guan et al. 2019), and the warm phase NAMV (referred to as NAMV+) is responsible for north-wet and south-dry anomalies in Europe during the 1990s and 1950s (Robson et al. 2012; Sutton and Hodson 2005; Sutton and Dong 2012). NA acts as a significant source of natural climate variability over the NA basin and adjacent

Accepted for publication in *Journal of Climate*. DOI10.1175/JCLI-D-19-0536.1.

continents (Ruprich-Robert et al. 2017), the increasing AMOC modulates the long-term loss of Arctic sea ice and northern hemisphere warming, especially in the late 1990s and early 2000s (Delworth et al. 2016). In addition, Atlantic multidecadal oscillation influences extratropical summertime rainfall in northwest Europe (Knight et al. 2006) with the NNAO (Sutton and Hodson 2005). Homoplastically, the multidecadal NA-SST also leads the NAO by approximately 15 years (Li et al. 2017), indicating the interaction and coupling effects of both NA-SST and NAO (Steinman et al. 2015; Jaime et al. 2017). NA-SST effects have been investigated by a coupled mode of NA tripole-NAO-AMOC (Li et al. 2017), identifying the multi-timescale effect of NAMV on Eurasian climate (Li et al. 2019).

From the perspective of NA-SST effect on extratropical extremes on the decadal timescale, NAMV+ closely corresponds to continued rise of extreme occurrences over Europe in the past 15-20 years (Seneviratne et al. 2014). Besides, the wave-energy anomaly related to extratropical extremes has been identified occurring over the NA (Screen and Simmonds 2013; Zhang et al. 2019). However, the NAMV effect on the summer extratropical extremes in other Eurasian regions is insufficient.

Accepted for publication in *Journal of Climate*. DOI10.1175/JCLI-D-19-0536.1.

To further reveal frequent extremes over Eurasian continent on the decadal timescale, this study explores the effect of NA-SST on the extratropical circulation and quasi-stationary waves at the decadal timescale, to facilitate extremes prediction.

Data and Methods

a. Data sources

Long-term monthly surface temperature and pressure-level atmospheric parameters are obtained from ERA-Interim for the period of 1979 to 2018 with a resolution of 1.5°×1.5 and accessed from http://apps.ecmwf.int/datasets/. Pressure-level atmospheric data is used for calculating wave activity flux; 200-hPa zonal wind U is used for reflecting jet distribution; 500-hPa and 300-hPa meridional wind V is used for exhibiting low frequency and amplitude of wave. To exhibit anomalies of extratropical circulation on the longer timescale beyond synoptic scale, quasi-stationary wave anomaly and the low-frequency waves are analyzed. The low-frequency wave index is defined as the average of the first two PCs of 500-hPa V wind in July and August (JA, 60°W–150°E, 20°N–60°N, Zhang et al. 2019), which

Accepted for publication in *Journal of Climate*. DOI10.1175/JCLI-D-19-0536.1.

explains 38.2% of the variance and reflects the variation of the mid-latitude Silk Road pattern (SRP).

Long-term monthly sea temperatures (with a resolution of 1.0°×1.0°) are obtained from the Met Office Hadley Centre website (https://www.metoffice.gov.uk/hadobs/, HadISST data), the SST data from 1950 to 2018 is used as climatological data for simulation, because the period is close to one period (65-80a) of NAMV. The NAMV index is defined as the low-pass filtered (trend begins in 1900) annual mean of area-averaged SST in the mid-high latitude NA (60°W–0°, 50°N–65°N), which is a key region for the NAMV, and the observed SST signal associated with the NAMV is strongest there (Sutton and Hodson 2005; Zhang et al. 2016). The time series of the 'AMOC fingerprint' is defined as the first leading principal component (PC1) of detrended subsurface ocean temperature anomalies at 400 m in the extratropical NA (80°W–0°, 20°N–65°N, Yan et al. 2017). The smoothed Atlantic multidecadal oscillation (AMO) index is retrieved from https://www.esrl.noaa.gov/psd/data/correlation/amon.sm.long.data based on the area-weighted average SST from Kaplan SST V2 over the NA from 0° to 70°N.

Accepted for publication in *Journal of Climate*. DOI10.1175/JCLI-D-19-0536.1.

Moreover, the NAO index is retrieved from https://crudata.uea.ac.uk/cru/data/nao/nao.dat, and is defined as the difference of pressure between Iceland and Gibraltar. The time period of both indices from 1979 to 2018 is used.

A self-calibrating Palmer drought severity index (sc-PDSI, Dai 2011) is a meteorological drought index with a 2.5°×2.5° resolution, and it provides a good reflection of soil moisture deficit or surplus, therefore it is widely used for drought/flood evaluation throughout the world. PDSI is obtained from the Climate Data Guide website (https://climatedataguide. ucar.edu/climate-data/palmer-drought-severity-index-pdsi). Severe drought is PDSI <=-3, severe flood is PDSI >=3; Extreme drought is PDSI <=-4, extreme flood is PDSI >=4. The extreme drought/flood is defined as the absolute PDSI larger than 3 in the study.

b. Statistical analyses

Given that there are zonal 6-8 wavenumbers in the mid-latitudes and zonal 4-6 wavenumbers in the high-latitudes, the JA amplitude is calculated using harmonic

Accepted for publication in *Journal of Climate*. DOI10.1175/JCLI-D-19-0536.1.

analysis and V wind (Screen and Simmonds 2013), JA amplitude is the summed amplitude for wavenumber m=6,7,8 at 300 hPa, as averaged over the 37.5°N-57.5°N latitudinal range; it reflects the amplitude variation of the low-frequency waves. Land-sea temperature contrast (LSTC) is defined as the surface temperature difference between European land (10°E-60°E, 35°N-65°N) and the mid-latitude NA (40°W-0°E, 35°N-65°N). We used empirical orthogonal function (EOF) analysis to display the spatial and temporal patterns of 200-hPa U wind, SST and 500-hPa V wind. The running means of the data are applied to obtain low-pass filtering of the variables. The statistical significance of the linear regression coefficient, anomaly field and the correlation between two series are assessed via a two-tailed Student's t-test and Monte Carlo test; Mann-Kendall mutation test is used. The correlations are from original series, with effective freedom of 40 (1979-2018).

The wave activity flux defined by Takaya and Nakamura (2001, defined as TNF) is applied to examine energy propagation of low-frequency wave and to reveal where anomalous wave energy is emitted, absorbed and transferred.

c. Models

Accepted for publication in *Journal of Climate*. DOI10.1175/JCLI-D-19-0536.1.

The linear baroclinic model (LBM) is employed to simulate atmospheric responses to an idealized forcing of diabatic heating and vorticity forcing over Europe. The LBM has a triangular truncation of 21 waves and a vertical resolution of 20 levels (Watanabe and Kimoto, 2000). The background state in the experiment is the JA climatology of 1979-2018 from the ECMWF/interim reanalysis. The forcing center of diabatic heating is over central Europe (50°N, 20°E), and vorticity forcing is over western Europe (50°N,10°E), with a horizontal scale of 12° ×6°, the vertical forcing is located at 700 hPa with 6 K/day and 10e-8 s^{-2}, and the integration time of the model is set to 30 days, and the data during the 15-30th days with steady state could be used for analyzing circulation characters.

The Community Earth System Model (CESM1.0, Hurrell et al. 2013) developed by the National Center for Atmospheric Research (NCAR) consists of interactively coupled models for the atmosphere (CAM), ocean (POP), land (CLM) and sea-ice (CICE). The model components are available at http://www.cesm.ucar.edu/models/cesm1.0/. The model is used to investigate the role of observed basin-scale SST patterns on amplitudes, summertime circulation and

Accepted for publication in *Journal of Climate*. DOI10.1175/JCLI-D-19-0536.1.

extremes. This analysis focuses on the influences of the NA-SST pattern. The SST boundaries are set to a 10° buffer of the southern boundaries over which the SST restoration, described below, ramps up from zero. The atmospheric component is the Community Atmospheric Model version 5.1 (CAM5.1) with the finite volume dynamic framework with a horizontal resolution of 1.9°×2.5° and 30 vertical layers of the $\sigma - p$ vertical coordinates. In this study, several physical processes, including radiation processes, cloud effects, convection, boundary layer effects etc. are represented in the model. Given that the PC1 exhibits a multi-decadal variation of SST, which shows significant correlation with NAMV index. In addition, as one sea surface pattern, EOF1 is influenced by sea-air interaction and vertical heat exchange between sea surface and deep sea, which will change SST pattern and heat distribution. Therefore, as for the sensitivity experiment of the SST forcing, double of the SST/EOF1 is taken as a hypothetical SSTA, and is superposed with the original climatological SST as the initial SST. Given that sea surface wind could modulates SST/EOF1 mode, the hypothetical SSTA is added to the SST for all months in summer since the second simulation year, so as to keep SST/EOF1 mode on the

Accepted for publication in *Journal of Climate*. DOI10.1175/JCLI-D-19-0536.1.

decadal timescales. The annual SST from the sensitivity experiment is contrasted with real SST field in recent two decades, it is within 0.4℃ variation, SST deviation on average between warm and cold phases, therefore, the forcing SST in the sensitivity experiment represents warm anomaly after 2000 and NAMV mode. A control simulation uses climatological SST from 1950 to 2018, which closes to SST during one period (65-80a) of NAMV, and its initial circulation fields use 40-yr climatological data (1979-2018). Both of sensitivity and control simulation run for 20a, with time increment of one day and monthly output data. The control SRP is the first leading EOF mode of 20-yr V wind under the climatological SST. The sensibility SRP is the first leading EOF mode of 20-yr V wind from the sensibility experiment. But as for difference between sensitivity and control experiments, the last 10-yr data are used.

Results

a. Increasing low-frequency wave contributions to the mid-latitude stationary wave amplitudes and extratropical extremes

Accepted for publication in *Journal of Climate*. DOI10.1175/JCLI-D-19-0536.1.

To elaborate extratropical extremes, the study selects six regions over Eurasian continent, those are western Europe (0-20°E, 40°N-55°N), eastern Europe (35°E-55°E, 45°N-60°N), central Asia (70°E-90°E, 40°N-55°N), East Asia (110°E-125°E, 35°N-55°N), central Russia (70°E-100°E, 60°N-70°N) and eastern Russia (120°E-150°E, 60°N-70°N). Fig.1 shows time series of extreme flood and drought frequency within 300 grids in JA, extreme droughts increase in western Europe, eastern Europe, East Asia, central Russia, and high frequency between 1970 and 2000 in eastern Russia; extreme floods increase in central Russia, eastern Russia and central Asia. Moreover, the total flood/drought trends indicate that an increase in western Europe, East Asia, central Russia and eastern Russia. Additionally, the trend and extreme frequency after 1990s shows increasing of extremes. The period analysis shows that those series of extremes have 14~21-yr period on the decadal timescale (figure omitted), the significant correlations of 21-yr smooth data indicates decadal variation of extremes, and it is enhancing stage after 1990s.

As for central Asia, although there is no significant increasing trend of the total droughts and floods, however, it is a significant increasing trend of floods, which is

Accepted for publication in *Journal of Climate*. DOI10.1175/JCLI-D-19-0536.1.

related to deepening wave trough around the Balkhash Lake, linking with enhancement in the quasi-stationary wave, and being favorable for precipitation and flood (Bothe et al. 2012); In addition, a branch of water vapor transport in central Asia is from Indian Ocean and Arabian Sea, therefore, the related subtropical circulations are also important for extremes (Huang et al. 2015), which results in complex variation of extremes in central Asia. As for eastern Europe, high frequency extremes mainly appear in 1972-1984 and 1996-2015, exhibiting a decadal variation. After 2000, there is an increasing trend of droughts, it is similar with the suggestion of Martin et al. (2018).

Fig.1 also marks selected extremes in six regions, with higher than mean frequency after 2000, significant extremes occurred in 2004, 2005, 2007, 2010, 2011 and 2012 in western Europe; 2002, 2004, 2005, 2009, 2010 and 2014 in eastern Europe; 2002, 2008, 2010, 2012 and 2013 in central Asia; 2001, 2002, 2004, 2005, 2006, 2007, 2009, 2010, 2011, 2012, 2013 and 2014 in East Asia; 2001, 2002, 2006, 2012 and 2013 in western Russia; 2001, 2003, 2004, 2006, 2007, 2008, 2010, 2013

Accepted for publication in *Journal of Climate*. DOI10.1175/JCLI-D-19-0536.1.

and 2014 in eastern Russia. Such large variabilities remind us that the extreme-related circulation is worthy of exploration.

Given that there are zonal 6-8 wavenumbers in the mid-latitudes (Screen and Simmonds 2013), and the quasi-resonant stationary wave links with extratropical extremes, Fig. 2. shows the time series of 5-8 wavenumber amplitudes in JA. The wave amplitude exhibits a low-frequency wave variation. The 6-8 wave component is very strong, with amplitudes at 300 hPa greater than averaged value after 2000, the amplitude is greater than 4 m/s during the extreme years, and the marked extremes are in 2001, 2002, 2003, 2007, 2009, 2010, 2011, 2012, 2015, 2017 with high frequency over the study area, which include widely concerned extremes in 2015 and 2017 in Eurasia (Garcia-Herrera et al., 2019; Zhang et al., 2019), heat wave in 2010 in Russia, and droughts in 2010 and 2012 in China, which is consistent with high wave amplitudes, indicating the possible linking with the high-amplitude. High amplitude reflects the contribution of transient waves (including free synoptic waves and low-frequency waves) and transient vorticity to quasi-stationary waves (e.g. climatology), due to spatially inhomogeneous diabatic sources/sinks and orography

Accepted for publication in *Journal of Climate*. DOI10.1175/JCLI-D-19-0536.1.

(Screen and Simmonds 2014). Increasing amplitudes favor increasing probability of high-frequency extremes, especially in the recent two decades. It is reasonable that quasi-resonance between free synoptic waves and quasi-stationary waves may lead to weather extremes, such as heat wave and flood, because many quasi-resonances occurs on the synoptic timescale, such as block high and cutting low (Hakkinen et al. 2011). However, how does quasi-resonance influence extremes on longer timescale such as extreme droughts? Extreme droughts are affected by persistent anomalies of atmospheric circulation, and it is a kind of climate extremes related to low-frequency variety of quasi-stationary waves. Thus, it is significant to explore climate extremes through quasi-stationary waves.

Such high-frequency in amplified wave amplitude after 2001 reveals that the decadal enhancement of quasi-stationary waves, which is possibly related to decadal forcing. The wave amplitude shows significant correlations with NAMV and AMOC at 90% confidence level (Fig.2a), which reflects the possible linkage with multidecadal NA-SST. Previous studies have suggested that low-frequency waves arise and magnify the amplitudes of the quasi-stationary waves (Coumous and

Accepted for publication in *Journal of Climate*. DOI10.1175/JCLI-D-19-0536.1.

Rahmstorf 2012; Coumous et al. 2014; Petoukhov et al. 2013; 2016), the related potential sources of which are the NA and Europe (Zhang et al. 2019). The low-frequency wave index is defined as the first two PCs of JA meridional wind in the mid-latitudes, which is used to reflect the intensity of SRP (Fig. 2b); the SRP intensity shows an enhancement after the 2001 and increasing intensity of the low-frequency waves. There are significant correlations of the low-frequency wave index with AMO and AMOC, indicating the possible linkage with the multidecadal NA-SST anomaly, and the significant correlation with wave amplitude shows the quasi-resonance effect of the low-frequency waves, and thereby magnify wave amplitude.

Fig. 3. shows mutation test of NA-SST related parameters, SRP and wave amplitude(A). The weak abrupt points of decadal changes of AMO/NAMV and AMOC begin in 1997, but the significant abrupt points are in 2000, 2003 and 2004, respectively. The abrupt points of SRP and wave amplitude occur in 2001-2004, which come after the abrupt points of NAMV/AMO and AMOC, indicating that decadal change of SRP and wave amplitude correspond to NA-SST pattern, with an

Accepted for publication in *Journal of Climate*. DOI10.1175/JCLI-D-19-0536.1.

adjusting stage of 2001-2004. How do the low frequency waves change with multidecadal NA SST? It is vital for evaluation and prediction of extratropical extremes.

b. Circulation anomalies and their relations with low-frequency waves and wave amplitude

To further identify the circulation anomalies after mutation stage and the enhanced quasi-stationary waves, Fig. 4a shows the difference of circulation-related factors in JA between 2001-2018 and 1979-2018. 200-hPa U deviations exhibit two positive anomaly centers (Fig. 4a); one is over the east coast of the mid-latitude NA, which casually occurs on the east and south flank of the NA jet exit and indicates southeast extension of the NA jet after 2001. The wave activity flux (defined as TNF) after 2001 also indicates a major divergent energy over the mid-latitude NA, and the wave activity flux is trapped into the Afro Asian jet (Fig. 4a). A north-south shift in the NA jet in summer is identified to link with floods in western Europe (Dong et al. 2013), record-breaking high temperatures in northeastern Europe (Mahlstein et al. 2012; Stadtherr et al. 2016), and heatwaves (Founda and Giannakopoulos 2009; Koutsias et

Accepted for publication in *Journal of Climate*. DOI10.1175/JCLI-D-19-0536.1.

al. 2012). On the other hand, a southeast shift in NA jet favors barotropic energy transfer to kinetic energy; and identically, southeast shift in NA jet is helpful to wave activity flux and energy disperse toward the Afro Asian jet, which acts as waveguide for the formation and enhancement of the low-frequency waves. And then the sinking energy could lead to circulation anomalies and extremes (Zhang et al. 2019). It also identifies the potential relationship between the NA jet anomaly and European extremes. Trouet et al. (2018) suggested an unprecedented increase in NA jet variance since the 1960s, therefore, its effect on extreme variation on the multi-timescale should be explored.

Fig. 4b shows deviation of surface temperature and 500-hPa geopotential height. Two temperature centers with significantly positive deviation are in the European continent and Greenland to the west of the NA; one center with negative deviation is in the mid-latitude NA. Surface temperature is influenced by atmospheric circulations, conversely, longitudinal temperature deviation forms a contrast of 'cooling ocean and warming land' pattern, influencing atmospheric circulations (Hoskins and Karoly 1981; He et al. 2018). Because the negative deviation of surface temperature is a

Accepted for publication in *Journal of Climate*. DOI10.1175/JCLI-D-19-0536.1.

section of NA-SST pattern on the multidecadal timescale, therefore, longitudinal temperature gradient relates to multidecadal NA-SST. In addition, positive/negative temperature centers correspond to anticyclone/cyclone anomalies described by geopotential height deviation, which corresponds to wave ridges/troughs by comparing with wave position, and reveals strengthening of the climatological wave ridges and wave troughs after 2001, as well as enhancement of quasi-stationary waves (Zhang et al. 2019). The latitudinal pattern of the geopotential height anomaly indicates an eastward shift of the NNAO pattern, due to a low-pressure anomaly over the west coast of North Europe.

We perform an EOF analysis for 200-hPa U wind to feature zonal wind and the NA jet anomaly. The first leading mode explains 33.3% of the total variance, and the mode exhibits a “-+-” latitudinal pattern (Fig. 5a), with positive values at the southeast of the NA jet exit and northern Europe. From the previous point of view, we can conclude that the JS shows a southeast extension NA-jet and a northwest shift of the entrance of Afro Asian jet in most recent decade, which favors the conjunction of two jets and strengthening of the Afro Asian jet waveguide. Moreover, the NA jet

Accepted for publication in *Journal of Climate*. DOI10.1175/JCLI-D-19-0536.1.

anomaly possibly increases barotropic energy transfer to kinetic energy, thereby enhances the low-frequency waves (Zhang et al. 2019). The first leading U/PC1 shows a multidecadal variation (Fig. 5b), which is closely related to wave amplitude (Fig. 5b), with a correlation coefficient of 0.28 at 90% confidence level, and has a significant correlation of 0.35 with the SRP at 95% confidence level. The results reveal that the southeast extension of NA jet in the 21st century well corresponds to magnified wave amplitude and intensity. Fig. 5b also exhibits a NNAO in the 21st century, with the abrupt point of decadal change in 2004, having a significant correlation coefficient of -0.54 with U/PC1 at 95% confidence level, and having a significant correlation of -0.29 with wave amplitude at a 90% confidence level. The relation between NA jet and NNAO emphasizes that NA jet position and speed variability is associated with the NNAO eddy-driven jet and the East Atlantic pattern (Woollings and Blackburn 2012; Hall et al. 2015). The abrupt point of U/PC1 is 2009, it is different from circulation and NA-SST mutation, which means that there are other effect factors that should be discussed.

c. LSTC and the relation with low-frequency wave and wave amplitude

Accepted for publication in *Journal of Climate*. DOI10.1175/JCLI-D-19-0536.1.

To feature the 'cooling ocean and warming land' pattern and its effect on the extratropical extremes, the study defines an LSTC indice (see method section). Fig. 6a shows a standardized LSTC indice in July and August (JA); both indices show significant increase trends, indicating increases in LSTC and longitudinal temperature contrast between the European continent and the NA, which may strengthen meridional wind and wave amplitudes according to thermal wind principle and a linearized nonstationary, nondivergent, barotropic vorticity equation (Hoskins and Karoly, 1981). Fig. 6b displays the time series of JA LSTC, which indicates a multidecadal variation with the abrupt point in 2004, and it has a correlation coefficient of 0.29 with the wave amplitude at 90% confidence level, and a significant correlation coefficient of 0.58 with the low-frequency wave indice at 95% confidence level. A significant increase in LSTC in the 21st century is helpful to the enhancement of meridional circulation, reflects enhancing in the low-frequency wave that imposed on the quasi-stationary wave, and further be helpful to the magnified amplitude of the quasi-stationary wave.

Accepted for publication in *Journal of Climate*. DOI10.1175/JCLI-D-19-0536.1.

To exhibit the effect of LSTC on atmosphere circulations, Fig. 6c shows the regression of the 500-hPa temperature (dT, shaded) and the geopotential height (contours) to the JA-LSTC indice. The significant anomaly centers of temperature exhibit wave patterns in the mid-latitude and high-latitude, with the negative centers over the North Atlantic and the positive centers over European continent, which correspond to the negative/positive centers of the geopotential height anomaly and the wave trough/ridge of the quasi-stationary wave, and the anomalous wave pattern due to LSTC possibly magnifies the amplitude of the quasi-stationary wave.

We also perform a correlation of the LSTC indice with the wave amplitude of the 5-8 wavenumbers (figure omitted) and find a significant correlations coefficient of 0.44 with the 7-wavenumber in August, and a correlation coefficient of 0.32 with the 8-wavenumber in July at 90% confidence level. These results further identify increase in the LSTC contributing to the magnified amplitude of the quasi-stationary wave.

d. Circulation anomalies and LSTC effects on the wave energy

To further identify the impact of the aforementioned three factors (southeast shift in NA-jet, NNAO, increasing LSTC) on the wave amplitude and intensity, the wave

Accepted for publication in *Journal of Climate*. DOI10.1175/JCLI-D-19-0536.1.

activity fluxes (TNFs) are regressed. The divergence wave activity flux is clear between the NA jet exit and the entrance of Afro Asian jet, but the effect various for each region due to different factors (Fig. 7). The significant regression TNFs to U/PC1 are mainly distributed between 20°W and 20°E along the NA jet, reflecting high divergence energy from NA jet exit and enhancement of wave disperse between two jets, which is helpful to reinforcing of the low frequency wave. The significant regression of TNF to -NAO covers a large range of jet belt between 60°W and 30°E along the NA jet and the Afro Asian jet, NNAO related vorticity favors baroclinic energy transfer (Zhang et al. 2019) because a cyclone anomaly related to NNAO just occurs over northwestern Europe, in front of the trough of the quasi-stationary wave, which leads to enhancement of convergence and ascending motion in the lower-middle troposphere, and thereby contributes to zonal configuration of warm-ascending and cool-descending that is helpful to baroclinic energy transfer. The significant regression of TNF to LSTC is mainly distributed between 40°W and 10°E along the NA jet, with a convergence TNF appearing over 10°W and the wave trough, which favors deepening of the wave trough and meridional wind. Increasing LSTC

Accepted for publication in *Journal of Climate*. DOI10.1175/JCLI-D-19-0536.1.

exhibited by the non-uniform longitudinal temperature gradient leads to meridional wind and wave enhancement according to the linearized nonstationary, nondivergent, barotropic vorticity equation (Hoskins and Karoly 1981) and thermal wind principle. All these TNF distributions reveal that different contribution of the three factors to wave energy and the low-frequency wave, and their effect mechanisms are worthy of further discussion.

To explore the jet and NNAO anomaly effect on energy conversion, we estimate energy conversion including the local barotropic energy conversion CK (Hoskins et al. 1983; Simmons et al. 1983) and local baroclinic energy conversion CP (Kosaka and Nakamura 2006).

$$CK = \frac{{v'}^2 - {u'}^2}{2}\left(\frac{\partial \bar{u}}{\partial x} - \frac{\partial \bar{v}}{\partial y}\right) - v'u'\left(\frac{\partial \bar{u}}{\partial y} - \frac{\partial \bar{v}}{\partial x}\right) \qquad (1)$$

$$CP = \frac{f}{\sigma} v'T' \frac{\partial \bar{u}}{\partial p} - \frac{f}{\sigma} u'T' \frac{\partial \bar{v}}{\partial p} \qquad (2)$$

where u' and v' are anomaly zonal and meridional wind velocity; $\bar{u}$ and $\bar{v}$ are the mean zonal and meridional wind velocity, respectively; T' is the anomaly temperature; f is the Coriolis parameter; $\sigma = \frac{R\bar{T}}{C_p p} - \frac{d\bar{T}}{dp}$ with temperature (T); and the specific heat at a constant pressure (C_p), p is pressure.

Fig.8 shows the 300-hPa barotropic energy (Fig.8a, CK) and 700-hPa baroclinic energy (Fig.8b, CP) after 2001, as well as the correlation between CK and jet anomaly

Accepted for publication in *Journal of Climate*. DOI10.1175/JCLI-D-19-0536.1.

(U/PC1, Fig.8c), and between CP and -NAO indice from 1979 to 2018 (Fig.8d). The reason to analyze 300-hPa CK is that it is close related to NA-jet anomaly, which is clear over upper troposphere; the reason to analyze 700-hPa CP is that lower-level baroclinicity is helpful to atmospheric stability and ascending motion, and it also corresponds to the effect of east extension of NNAO.

The positive CK at the NA jet exit to the entrance of the Afro Asian jet indicates the barotropic energy conversion. The positive correlation between CK and U/PC1 at the NA jet exit shows that increasing U wind and southeast extension of NA jet favors barotropic energy conversion from background state to seasonal kinetic energy.

Along the west coast of northwest Europe, positive baroclinic energy observed after 2001, which reflects increasing baroclinic condition, corresponding to cyclone anomaly and eastward shift in NNAO. The correlation between CP and -NAO shows positive correlation over Europe, indicating increase of baroclinic energy conversion to seasonal kinetic energy, corresponding to NNAO. The reason is that east extension of NNAO appears over the west coast of northwest Europe, in front of stationary wave trough with baroclinicity, which is favorable for ascending motion, such

Accepted for publication in *Journal of Climate*. DOI10.1175/JCLI-D-19-0536.1.

baroclinicity configuration with zonal warm-ascending and cold-descending favors baroclinic energy conversion to kinetic energy. The kinetic energy enhances wave activity motion and wave energy dispersing along jet waveguide, it is the same as regression of wave activity motion to –NAO in Fig.7b.

The results reveal that southeast extension of NA jet and NNAO favor increasing barotropic and baroclinic energy conversion to kinetic energy, which is helpful to enhancement of wave activity motion and the low frequency waves.

e. Effects of SST pattern on the circulation and LSTC anomaly

Strengthened NA jet have been suggested to link with variances in the central NA and NA basins (Black et al. 2014; Liu et al. 2017; Trouet et al. 2018), as well as warming in Europe (Sun, 2014), because of zonal non-uniform heating and the thermal wind principle, except for dynamic processes of the eddy vorticity flux. We investigate the linkages of the NA-SST with NA jet, NAO and LSTC, and the first SST leading mode explains 40.2% of the total variance (Fig. 9a); the mode exhibits a "+-+" latitudinal pattern, with weakly negative anomaly in the mid-latitude NA (40°N -60°N) at the southeast of the NA jet exit, and with the positive anomaly across other

Accepted for publication in *Journal of Climate*. DOI10.1175/JCLI-D-19-0536.1.

regions of the NA (20°N -80°N). Fig. 9b indicates that the NA-SST /PC1 correlates with the U/PC1, NAO and LSTC, with significant correlation coefficients of 0.32, -0.57 and 0.33 at 95% confidence level, respectively, and this indicates that the NAMV pattern with '+-+' zonal pattern is possibly related to the eastward shift in the NNAO, due to a low pressure anomaly over south of Iceland; and there is a zonal SST mode of the mid-cooling and south-warming on the south flank of NA jet exit, which is helpful for southward shift in NA-jet, based on thermal wind principle. According to Fig. 7 and Fig. 8, anomalies of NNAO and southward shift in NA-jet closely relate to barotropic/baroclinic energy transfer to kinetic energy which thereby excites and enhances the low-frequency waves. The NAMV SST pattern with '+-+' zonal pattern possibly contributes to increase in LSTC in 2000s, because of cooling mid-latitude NA and NAMV effect on warming central Europe (Sutton et al. 2005; 2012).

Fig. 9b shows low-pass filtered AMO, AMOC and NAMV index during the entire period of 1979–2018. The SST/ PC1 pattern is well correlated with the original NAMV index (Sutton and Hodson, 2005), AMO and AMOC, with correlation coefficients of 0.8, 0.82 and 0.66, respectively. AMO could explain some interdecadal

Accepted for publication in *Journal of Climate*. DOI10.1175/JCLI-D-19-0536.1.

components of summer hot days and heatwaves in subtropical regions for 1979–2016 (Kushnir 1994; Zhang et al. 2018). However, explanations for AMO and extratropical extremes are lacking. The significant correlation of NAMV with the SST/PC1 pattern reveals that SST/ EOF1 pattern could reflect multidecadal variation of the mid-high latitude NA-SST, through circulation anomalies such as eastward extension of NNAO, southeast shift in NA-jet, increasing LSTC and so on, SST/EOF1 pattern links to the extremes-related amplitude of waves (Fig. 2).

AMOC anomalies at the mid-high latitudes have been observed to lead the fingerprint by ~4 years with respect to the mid-lower latitude fingerprint as a proxy for AMOC variations (Smeed et al. 2014) due to the slow propagation of heat transport (Zhang and Zhang 2015). The correlation of leading AMOC index with the SST/PC1 pattern shows a significant correlation. Previous study has shown that the AMOC stores approximately one-half of global excess heat during an accelerating phase from the mid-1990s to the early 2000s, which contributes to the global-warming slowdown in the beginning of the 21st century (Chen and Tung 2018). It is expected that an intensified AMOC lasts at least for approximately two decades,

Accepted for publication in *Journal of Climate*. DOI10.1175/JCLI-D-19-0536.1.

which will further result in low-level oceanic heat uptake manifesting as a period of rapid global surface warming, as well as favoring persistence of the NAMV SST pattern.

Fig. 9c-d shows regressions of 200-hPa U, 500-hPa geopotential height and surface temperature to the NA-SST/PC1. The U anomaly related to the SST pattern exhibits a '-+-' zonal pattern over NA and Europe with a positive anomaly at the exit of NA jet to northern Europe and a negative anomaly over southern Europe and northern NA jet, which exhibits the southeast extension of the NA jet exit and the northward extension of the entrance of Afro Asian jet. The regression of the geopotential height anomaly likes the eastward shift in the NNAO pattern (Fig. 9d), which is consistent with recent decadal anomalies of NAO (Ulbrich and Christoph 1999). On the one hand, such pattern identifies a cyclone anomaly over western Europe, on the other hand, the cyclone leads to the eddy-driven jet effect on the southeast extension of the NA jet exit. The regression of surface temperature (Fig. 9d) exhibits a negative anomaly in the mid-latitude NA and a positive anomaly in eastern Europe, which is manifested as a 'cooling ocean and warming land' pattern in the mid-latitude, shows a positive

Accepted for publication in *Journal of Climate*. DOI 10.1175/JCLI-D-19-0536.1.

anomaly of LSTC during the early 21st century. The regression maps also reveal a low-frequency wave pattern (figure omitted), which is close to the quasi-stationary wave with similar wavenumber.

Fig. 9 indicates that the NAMV SST pattern could represent multidecadal change of NA-SST, and it is possibly favorable for multidecadal variability of southeast extension of the NA jet, the eastward shift in the NNAO and the increasing in LSTC. Conversely, previous research has shown that multidecadal variations of NAO can induce multidecadal variations in the AMOC and poleward ocean heat transport in the Atlantic (Smeed et al. 2014), which dominates long-term high-latitude SST and the Arctic, superimposed on long-term anthropogenic forcing. In addition, poleward shifts in the NA jet in the future correspond to increased anthropogenic forcing (Iqbal et al. 2017). Those reveal that multidecadal variability of the mid-high latitude circulations are the result of air-sea interaction, ocean dynamics and thermodynamics, superimposed on long-term anthropogenic forcing, except for the remote forcing of tropical SST pattern (Okumura, et al. 2001; Zhang et al. 2019). These multidecadal

Accepted for publication in *Journal of Climate*. DOI10.1175/JCLI-D-19-0536.1.

circulation anomalies in the mid-high latitude act as the background of frequent extratropical extremes on the multidecadal timescale.

f. Simulation of increase in the LSTC and NNAO related vorticity anomaly

To identify the magnifying wave amplitude due to a non-uniform temperature distribution and the increasing LSTC, this study conducts one experiment related to the longitudinal non-uniform temperature. A forcing of diabatic heating is performed over Europe (center: 50°N, 20°E) at 700 hPa. In addition, to identify the contribution of eastward shift in NNAO, corresponding to the cyclone anomaly over western Europe, another experiment is positive vorticity forcing (center: 50°N, 10°E) conducted at 700 hPa (schemes are shown in model section).

The simulation results show that diabatic heating and positive vorticity forcing are similar in the mid-latitude. Both of them are favorable for two significant wave patterns exhibited by geopotential height over the mid-latitude and high latitude (Fig. 10a-b). The anticyclone and cyclone anomalies correspond to the wave ridge and trough of the quasi-stationary wave, which indicates that the LSTC related diabatic heating and the NNAO related vorticity forcing could excite the low frequency waves,

Accepted for publication in *Journal of Climate*. DOI10.1175/JCLI-D-19-0536.1.

with the same phase and wavenumbers as the quasi-stationary wave, which favors for resonant probability.

From the jet perspective, the Afro Asian jet exhibits shrinking and a decreasing of 20 m/s zonal winds from central Asia to southern Mediterranean Sea and northern Africa under the vorticity forcing. But an increase of 20 m/s zonal winds over Europe and the east coast of the North Atlantic under the LSTC related diabatic forcing. These findings indicate a northward shifting in the entrance of the Afro Asian jet. Besides, there are significant eastward extension of 20m/s U wind, which indicates an eastward extension of the NA jet exit due to NNAO eddy-driven jet. Moreover, the jet anomaly is conducive to an increase in energy transfer from the background to kinetic energy and energy disperse trapped into the Afro Asian jet, and the jet waveguide favors warming over Europe (Branstator 2002; Wang et al. 2014). On the other hand, NNAO is favorable for a low frequency wave exhibited by a geopotential height anomaly, such as blockings (He et al. 2018). The simulation results agree with above diagnostic analysis, which further identify that the LSTC related diabatic heating and

Accepted for publication in *Journal of Climate*. DOI10.1175/JCLI-D-19-0536.1.

NNAO related vorticity anomalies may excite the low frequency wave along two jets and magnify amplitude of the quasi-stationary wave.

g. Simulation of the NA-SST pattern effect on extremes

To further quantify the magnification of wave magnitude, intensity and relations with the intensified NAMV related SST mode, SST forcing in the sensitivity experiment has been conducted by combining double of the first leading SST mode with climatological SST and annual simulated SST in summer (the description is in model section). The key circulation anomalies such as jet anomaly, NAO pattern and LSTC, are analyzed. 200-hPa U wind from sensitivity experiment shows a positive anomaly at the NA jet exit and north of the entrance of the Afro Asian jet (Fig. 11a), which indicates a southeast extension of the NA jet. Such anomalies could well conjunct the NA jet with the Afro Asian jet, thereby enhance the jet waveguide between two jets. From the energy perspective, the U wind deviation could change the interaction between background and seasonal energy transfer (Hoskins and Karoly 1981), and further results in increasing seasonal kinetic energy. The wave activity flux at the 200-hPa level (Fig. 11a) further certifies the divergence energy in the

Accepted for publication in *Journal of Climate*. DOI10.1175/JCLI-D-19-0536.1.

positive U region and the NA jet exit. Moreover, wave energy disperses along the Afro Asian jet and the subpolar jet, which favors enhancement of the low frequency waves.

The anticyclone/cyclone anomalies that correspond to the SST/ PC1 pattern are exhibited by the geopotential height anomalies (Fig. 11b), which exhibit an eastward shift of NNAO-like pattern described by the latitudinal pattern of cyclone anomalies over northwestern Europe and anticyclones over Greenland. NAO-like eddies also contribute to an extension of high-frequency eddies that drive the jet (Vries et al. 2013). The meridional pattern of cyclone anomalies over northwestern Europe and western Siberia and anticyclones over eastern Europe and eastern Siberia indicate a wave train, the cyclone/anticyclone anomalies correspond to wave troughs/ridges of the quasi-stationary waves, and favor increasing amplitudes of the quasi-stationary waves. The surface temperature anomalies corresponding to the SST/PC1 pattern, show a meridional wavelike pattern (Fig. 11c) with a negative anomaly over the mid-latitude NA to western Europe and East Asia and positive anomalies over central Europe to central Asia. The pattern reveals that NAMV could contribute to the

Accepted for publication in *Journal of Climate*. DOI10.1175/JCLI-D-19-0536.1.

‘cooling ocean and warming land’ pattern, in addition to the Europe warming under global warming (Dong and Sutton 2013). The pattern favors enhancement of meridional circulation and increasing amplitude of the quasi-stationary wave. Besides, the anticyclone anomaly around the Ural mountain favors the enhancement and eastward of Ural blocking high (Matsueda, and Endo 2017), which explains some extremes over Eurasia (García-Herrera et al. 2019).

To emphasize the difference between the control SRP and the sensitivity SRP, the first V-wind leading modes (20°N-60°N, 30°W-150°E) in JA from control and sensitivity simulation are performed. The centers of V-wind mode are connected(Fig.12a), which represents the climatological SRP, NAMV-related SRP pattern and SRP pathways. From the perspective of SRP pathways, there is a northward shift of the sensitivity SRP wave over the Eurasian continent, by comparing with control SRP, which reveals the magnified wave amplitude that enhances north wind and the anticyclone anomaly over North China and enhances extreme droughts (Zhang et al. 2019). The positive-negative centers of V-wind mode reflect SRP phase. By comparing the SRP phases, it is found that there is east shift in

Accepted for publication in *Journal of Climate*. DOI10.1175/JCLI-D-19-0536.1.

SRP centers between 40°N -50°N and the high latitude (50°N -70°N) on the east of 60°E, with less than quarter period, which reveals eastward shift of climate anomaly corresponding to the eastward NNAO and the southeast extension of the NA jet. Moreover, eastward shift in the wave pattern could explain the eastward Ural blocking high (Matsueda, and Endo 2017; García-Herrera et al. 2019). However, west shifts of SRP centers occur over NA and north Europe between 50°N -70°N. Therefore, the phenomenon shows a complex relation between the physical process of SRP shift and NNAO and eastward extension of NA jet, which needs further discussion.

To further identify the contributions of the intensified NAMV related SST mode to the wave amplitude and extratropical extremes, the time series of wave amplitude from the 20-yr control simulation and sensitivity simulation are calculated. The circulation-parameters in the first year are replaced with the mean value of 20-yr control simulations before calculating wave amplitude, acting as a reference. Considering the close phase (less than quarter period) of wavelike circulation between control and sensibility results, the standardized difference between sensitivity and

Accepted for publication in *Journal of Climate*. DOI10.1175/JCLI-D-19-0536.1.

control is showed (Fig. 12b). To feature SRP intensity, the standardized V/PC1 series from sensitivity and control are showed in Fig. 12b, which represent wave intensity. The results show that the wave intensity under the control simulation is close to the mean value of control simulation, however, most of them are higher in the sensitivity experiment than the control, and the wave amplitude from sensitivity experiment is also higher than control experiment, especially after the ninth years, revealing increase in wave intensity and wave amplitude, due to increasing in intensified NAMV. The simulated result is in accordance with the above diagnostic analysis.

Summary and Discussion

The magnification of wave magnitude is identified to closely relate to extratropical extremes. The causes of decadal-scale increase in extremes in the 21st century is still uncertainty, although many materials have discussed the extremes under global warming (Palmer et al 2002; Francis and Vavrus, 2012; Huang et al. 2017; Johnson et al. 2018). From the perspective of internal variability of earth-atmospheric interaction system, the NAMV is an important forcing due to its impact on the widespread atmospheric quasi-stationary wave at the multidecadal timescale. This study reveals

Accepted for publication in *Journal of Climate*. DOI10.1175/JCLI-D-19-0536.1.

the linkage of NAMV and the anomalies of quasi-stationary wave with respect to the following three aspects: 1) Intensified NAMV with zonal ‘+-+’ SST mode favors southeast extension of the NA jet, according to thermal wind principle; 2) Intensified NAMV with zonal ‘+-+’ pattern and positive anomaly temperature over the mid-high latitude is helpful to zonal pressure anomaly, which possibly favors the eastward shift in the NNAO pattern, and thereby strengthens eddy disturbance over western Europe and enhances the eddy driven jet, contributing to southeast extension of the NA jet; 3) Intensified NAMV with cool mid-latitude SST and NAMV effect on warming Europe contributes to the mid-latitude ‘cooling ocean and warming land’ pattern, which increases meridional circulation and meridional wind, according to V-wind thermal wind principle and barotropic vorticity equation (Hoskins and Karoly 1981).

The magnification of wave magnitude is identified to link to the decadal anomaly of the southeast extension of the NA jet, increasing LSTC, the eastward shift in NNAO, and so on. The schematic diagram (Fig. 13) shows the mechanism of the NA-SST pattern effect on the low-frequency waves and the magnification amplitude of the quasi-stationary wave. Three physical processes are marked. a) Southeast

Accepted for publication in *Journal of Climate*. DOI10.1175/JCLI-D-19-0536.1.

extension of NA jet anomaly favors barotropic energy transfer to seasonal kinetic energy and waveguide between NA jet and Afro Asian jet, which enhances jet stream waviness (Francis and Vavrus 2012) by altering in jet width, position and intensity. b) Eastward shift in NNAO is helpful to baroclinic energy conversion to seasonal kinetic energy, as well as eddy driven jet; both processes lead to increasing in energy transfer and disperse, which excites or enhances the low frequency wave. c) Increasing in LSTC leads to enhancement of meridional wind, which enhances amplitude of the low frequency wave. The reinforcing low frequency waves increases quasi-resonance probability and amplifies amplitude of the quasi-stationary wave (Dong et al. 2013), which thereby favors extratropical extremes with high frequency in summer.

Similar to the NA jet anomaly, the latitudinal position anomaly of the North Pacific jet (Shaman et al. 2009; Belmecheri et al. 2017) is also changed. However, the linkage of the North Pacific jet anomaly with extratropical extremes and the relationships between the NA jet and the North Pacific jet receive less attention. Except for NAMV pattern, NNAO can also lead to cooling of the mid-latitude

Accepted for publication in *Journal of Climate*. DOI10.1175/JCLI-D-19-0536.1.

NA-SST (Delworth et al. 2016), which also favors increasing in LSTC, and further explains the low-frequency wave anomalies. The study just discusses NA-SST effect on the extremes on the multidecadal scale, however, it is significant to further discuss other internal variabilities of earth-atmospheric system and anthropogenic warming. Because of lagging behind NAMV mutation of the decadal change of the above three factors and wave parameters (amplitude and intensity), it is inferred a coupling effect of NAMV and other forcing should be further explored.

Acknowledgments

This research was jointly supported by the National Key R&D Program of China (Grant No. 2016YFA0600702; 2018YFC1507101), the National Natural Science Foundation of China (Grant No. 41630426, 41975083) and Distinguished Young Scientists (Grant No. 41625019).

References

Baines, P. G. and C. K. Folland, 2007: Evidence for a rapid global climate shift across the late 1960s. *J. Clim.*, **20**, 2721–44.

Accepted for publication in *Journal of Climate*. DOI10.1175/JCLI-D-19-0536.1.

Belmecheri, S., F. Babst, A. R. Hudson, J. Betancourt, and V. Trouet, 2017: Northern Hemisphere jet stream position indices as diagnostic tools for climate and ecosystem dynamics. *Earth Interact,* **21**, 1–23.

Black, B. A. et al., 2014: Six centuries of variability and extremes in a coupled marineterrestrial ecosystem. *Science,* **345**, 1498–1502.

Booth, B. B. B., N. J. Dunstone, P. R. Halloran, R. Andrews, and N. Bellouin, 2012: Aerosols implicated as a prime driver of twentieth-century North Atlantic climate variability. *Nature*, **484**, 228–232.

Bothe, O., K. Fraedrich, X. Zhu, 2012: Precipitation climate of Central Asia and the large-scale atmospheric circulation. *Theoretical & Applied Climatology*, **108**(3-4): 345–354.

Branstator, G. 2002: Circumglobal teleconnections, the jet stream waveguide, and the North Atlantic Oscillation. *J. Clim.,* **15**,1893–1910.

Chang, C. Y., J. C. H. Chiang, M. F. Wehner, A. R. Friedman, and R. Ruedy, 2011: Sulfate aerosol control of tropical Atlantic climate over the twentieth century. *J. Clim.,* **24**, 2540–2555, doi:10.1175/2010JCLI4065.1.

Accepted for publication in *Journal of Climate*. DOI10.1175/JCLI-D-19-0536.1.

Chen, X. and K. K. Tung, 2018: Global surface warming enhanced by weak Atlantic overturning circulation. *Nature,* **559**, 387–391.

Clement, A. et al., 2015: The Atlantic multidecadal oscillation without a role for ocean circulation. *Science,* **350**, 320–324.

Coumou, D. and S. Rahmstorf, 2012: A decade of weather extremes. *Nat. Clim. Chang*, **2**(7),491–496.

Coumou, D., V. Petoukhov, S. Rahmstorf, S. Petri, and H. J. Schellnhuber, 2014: Quasi-resonant circulation regimes and hemispheric synchronization of extreme weather in boreal summer. *Proc Natl Acad Sci*., **111**(34), 12331.

Coumou, D., J. Lehmann, and J. Beckmann, 2015: The weakening summer circulation in the Northern Hemisphere mid-latitudes. *Science*, **348**(6232), 324–327.

Dai, A., 2011: Characteristics and trends in various forms of the Palmer drought severity index during 1900–2008. *J. Geophys. Res.*, **116**, D12115, doi:10.1029/2010JD015541.

Accepted for publication in *Journal of Climate*. DOI10.1175/JCLI-D-19-0536.1.

Delworth, T. L. and M. E. Mann, 2000: Observed and simulated multidecadal variability in the Northern Hemisphere. *Clim. Dyn.*, **16**(9), 661–676.

Delworth, T. L., F. Zeng, G. A. Vecchi, X. Yang, L. Zhang, and R. Zhang, 2016: The North Atlantic Oscillation as a driver of rapid climate change in the Northern Hemisphere. *Nature Geoscience*, **9**, 509–512.

Dong, B. W., R. T. Sutton, T. Woollings, and K. Hodges, 2013: Variability of the NA summer storm track: mechanisms and impacts on European climate. *Env. Res. Lett.*, **8**, 034037.

Drews, A. and R. J. Greatbatch, 2016: Atlantic Multidecadal Variability in a model with an improved North Atlantic Current. *Geophys. Res. Lett.*, **43**, 8199–8206.

Eden, C. and T. Jung, 2001: North Atlantic interdecadal variability: Oceanic response to the North Atlantic Oscillation (1865-1997). *J. Clim.*, **14,** 676–691.

Francis, J. A. and S. J. Vavrus, 2012: Evidence linking Arctic amplification to extreme weather in mid-latitudes. *Geophys. Res. Lett.*, **39**, L06801.

Francis J.A. and S.J. Vavrus, 2015: Evidence for a wavier jet stream in response to rapid Arctic warming. *Environ Res Lett.*, **10**(1), 014005.

Accepted for publication in *Journal of Climate*. DOI10.1175/JCLI-D-19-0536.1.

Folland, C. K., J. Knight, H. W. Linderholm, D. Fereday, S. Ineson, and J. W. Hurrell, 2009: The Summer North Atlantic oscillation: past, present, and future. *J. Clim.*, **22**,1082–1103. doi:10.1175/2008JCLI2459.1.

Founda, D. and C. Giannakopoulos, 2009: The exceptionally hot summer of 2007 in Athens, Greece - a typical summer in the future climate? *Glob. Planet. Change,* **67**, 227–236.

García-Herrera, R., J. Garrido-Perez, D. Barriopedro, C. Ordóñez, S. Vicente- Serrano, R. Nieto, L. Gimeno, R. Sorí, and P. Yiou, 2019: The European 2016/2017 drought. *J. Clim.*, doi:10.1175/JCLI-D-18-0331.1.

Goldenberg, S. B., C. W. Landsea, A. M. Mestas-Nun˜ez, and W. M. Gray, 2001: The recent increase in Atlantic hurricane activity: Causes and implications, *Science*, **293**, 474– 479.

Guan, X., J. Ma, J. Huang, R. Huang, L. Zhang and Z. Ma, 2019: Impact of oceans on climate change in drylands. *Science China Earth Sciences*, **62**, 891–908. DOI: org/10.1007/s11430-018-9317-8.

Accepted for publication in *Journal of Climate*. DOI10.1175/JCLI-D-19-0536.1.

Häkkinen, S., P. B. Rhines, and D. L. Worthen, 2011: Atmospheric blocking and Atlantic multi-decadal ocean variability. *Science,* **334**, 655–660, doi:10.1126/science.1205683.

Hall, R., R. Erdelyi, E. Hanna, J. M. Jones, and A. A. Scaife, 2015: Drivers of North Atlantic Polar Front jet stream variability. *I. J. Climatol.,* **35**, 1697–1720.

He, Y., J. Huang, D. Li, et al. 2018: Comparison of the effect of land-sea thermal contrast on interdecadal variations in winter and summer blockings. *Clim. Dyn.,* **51**,1275–1294.

Hong, C., H. Hsu, N. Lin, and H. Chiu, 2011: Roles of European blocking and tropical-extratropical interaction in the 2010 Pakistan flooding. *Geophys Res. Lett.,* **38**(13), L13806.

Hoskins, B. J. and D.J. Karoly, 1981: The steady linear response of a spherical atmosphere to thermal and orographic forcing. *J. Atmos. Sci.,* **38**(6), 1179–1196.

Huang, J., H. Yu, X. Guan, G. Wang, and R. Guo, 2016a: Accelerated dryland expansion under climate change. *Nature Clim. Change,* **6**(2), 166–172.

Accepted for publication in *Journal of Climate*. DOI10.1175/JCLI-D-19-0536.1.

Huang, J., M. Ji, Y. Xie, S. Wang, Y. He and J. Ran, 2016b: Global semi-arid climate change over last 60 years. *Clim. Dyn.*, **46**, 1131–1150. DOI:10.1007/s00382-015-2636-8.

Huang, J., H. Yu, A. Dai, Y. Wei, and L. Kang, 2017: Drylands face potential threat under 2°C global warming target. *Nature Clim. Change*, doi: 10.1038/NCLIMATE3275.

Huang, J., J. Ma, X. Guan, Y. Li, and Y. He, 2019: Progress in semi-arid climate change studies in China. *Adv. Atmos. Sci.*, **36**, 922–937. DOI: 10.1007/s00376-018-8200-9.

Huang, W., S. Feng, J. Chen and F. Chen, 2015: Physical Mechanisms of Summer Precipitation Variations in the Tarim Basin in Northwestern China. *J. Clim.*, **28**(9), 3579–3591.

Hurrell, J. W., M. M. Holland, and P. R. Gent, 2013: The Community Earth System Model: a framework for collaborative research. *Bull. Am. Meteorol. Soc.*, **94**, 1339–1360.

Accepted for publication in *Journal of Climate*. DOI10.1175/JCLI-D-19-0536.1.

Iqbal, W., W. N. Leung, and A. Hannachi, 2017: Analysis of the variability of the North Atlantic eddy-driven jet stream in CMIP5. *Clim. Dyn.,* https://doi.org/10.1007/ s00382-017-3917-1.

Jaime, Madrigal-González, Ballesteros-Cánovas, A. Juan, A. Herrero, P. Ruiz-Benito, M. Stoffel, and M. E. Lucas-Borja, 2017: Forest productivity in southwestern europe is controlled by coupled north atlantic and atlantic multidecadal oscillations. *Nature Comm.*, **8**(1), 2222.

Johnson, N. C., S. P. Xie, Y. Kosaka, and X. Li, 2018: Increasing occurrence of cold and warm extremes during the recent global warming slowdown. *Nat. Comm.*, **9**(1), 1724.

Kerr, R., 2000: A North Atlantic climate pacemaker for the centuries. *Science*, **288**, 1984–1985, doi:10.1126/science.288.5473.1984.

Knight, J. R., C. K. Folland, and A. A. Scaife, 2006: Climate impacts of the Atlantic multidecadal oscillation. *Geophys Res. Lett.,* **33**(17), DOI:10.1029/2006GL026242.

Accepted for publication in *Journal of Climate*. DOI10.1175/JCLI-D-19-0536.1.

Koutsias, N., M. Arianoutsou, A. S. Kallimanis, G. Mallinis, J. M. Halley, and P. Dimopoulos, 2012: Where did the fires burn in Peloponnisos, Greece the summer of 2007? Evidence for a synergy of fuel and weather. *Agr. For. Meteorol.*, **156**, 41–53.

Kushnir, Y., 1994. Interdecadal variations in North Atlantic sea surface temperature and associated atmospheric conditions. *J. Clim.*, **7**, 141–157.

Li, H., H. Chen, H. Wang, J. Sun, J. Ma, 2018: Can Barents Sea ice decline in spring enhance summer hot drought events over northeastern China? *J. Clim.*, **31**(12), 4705–4725.

Li, J., C. Sun, and F. Jin, 2017: A Decadal-scale Air-sea Interaction Theory for North Atlantic Multidecadal Variability: the NAT-NAO-AMOC-AMO Coupled Mode and Its Remote Influences. *Geophysical Research Abstracts*, **19**, 2017–5987.

Li, J. P., and C. Q. Ruan, 2018: The North Atlantic-Eurasian teleconnection in summer and its effects on Eurasian climates. *Envir. Res. Lett.*, **13**, 024007, https://doi.org/ 10.1088/1748-9326/aa9d33.

Accepted for publication in *Journal of Climate*. DOI10.1175/JCLI-D-19-0536.1.

Li, J. P., F. Zheng, C. Sun, J. Feng, and J. Wang, 2019: Pathways of influence of the Northern Hemisphere mid-high latitudes on East Asian climate: A review. *Adv. Atmos. Sci.*, **36**(9), 902–921.

Liu, Y., K. M. Cobb., H. Song, et al., 2017: Recent enhancement of central Pacific El Nino variability relative to last eight centuries. *Nat. Comm.,* **8**, 15386.

Mahlstein, I., O. Martius, C. Chevalier, and D. Ginsbourger, 2012: Changes in the odds of extreme events in the Atlantic basin depending on the position of the extratropical jet. *Geophys. Res. Lett.,* **39**, L22805.

Martin, H., R. Oldrich, M. Yannis, Máca Petr, S. Luis, K. Jan, and K. Rohini, 2018: Revisiting the recent European droughts from a long-term perspective. *Sci. Rep.*, **8**(1), 9499–9503.

Matsueda, M. and H. Endo, 2017: The robustness of future changes in Northern Hemisphere blocking: a large ensemble projection with multiple sea surface temperature patterns. *Geophys. Res. Lett.,* **44**, 5158–66.

Accepted for publication in *Journal of Climate*. DOI10.1175/JCLI-D-19-0536.1.

Okumura, Y., S. P. Xie, A. Numaguti, and Y. Tanimoto, 2001: Tropical atlantic air-sea interaction and its influence on the NAO. *Geophys. Res. Lett.,* **28**(8), 1507–1510.

O'Reilly, C. H., M. Huber, T. Woollings, and L. Zanna, 2016: The signature of low frequency oceanic forcing in the Atlantic Multidecadal Oscillation. *Geophys. Res. Lett.,* **43**, 2810–2818.

Otterå, O. H., M. Bentsen, H. Drange, and L. Suo, 2010: External forcing as a metronome for Atlantic multidecadal variability. *Nat. Geosci.*, **3**, 688–694, doi:10.1038/ngeo955.

Palmer, T. N. and J. Räisänen, 2002: Quantifying the risk of extreme seasonal precipitation events in a changing climate. *Nature*, **415**, 512–514.

Petoukhov, V., S. Rahmstorf, S. Petri, and H. J. Schellnhuber, 2013: Quasiresonant amplification of planetary waves and recent Northern Hemisphere weather extremes. *Proc Natl Acad Sci*., **110**(14), 5336–5377.

Petoukhov, V., S. Petri, S. Rahmstorf, D. Coumou, K. Kornhuber, and H. J. Schellnhuber, 2016: Role of quasiresonant planetary wave dynamics in recent

Accepted for publication in *Journal of Climate*. DOI10.1175/JCLI-D-19-0536.1.

boreal spring-to-autumn extreme events. *Proc Natl Acad Sci*., **113** (25), 6862–6867.

Robson, J., R. Sutton, K. Lohmann, D. Smith, and M. Palmer, 2012: The causes of the rapid warming of the North Atlantic Ocean in the mid 1990s. *J. Clim.,* **25**, 4116–4134.

Ruprich-Robert, Y., F. Msadek Castruccio, S. Yeager, T. Delworth, G. Danabasoglu, 2017: Assessing the climate impacts of the observed Atlantic multidecadal variability using the GFDL CM2.1 and NCAR CESM1 global coupled models. *J Clim.,* **30**,2785–2810.

Sutton, R. T. and B. Dong, 2012: Atlantic Ocean influence on a shift in European climate in the 1990s. *Nat. Geosci.,* **5**,788–792.

Schlesinger, M. E. and N. Ramankutty, 1994: An oscillation in the global climate system of period 65-70 years. *Nature,* **367**,723–726.

Schlesinger, M. E. and N. Ramankutty, 1994: An oscillation in the global climate system of period 65–70 years. *Nature,* **367**, 723–726.

Accepted for publication in *Journal of Climate*. DOI10.1175/JCLI-D-19-0536.1.

Screen, J. A. and I. Simmonds, 2013: Exploring links between Arctic amplification and mid-latitude weather. *Geophys Res. Lett.*, **40,** 959–64.

Screen, J. A. and I. Simmonds, 2014: Amplified mid-latitude planetary waves favour particular regional weather extremes. *Nat. Clim. Change*, 4, 704–709.

Seneviratne, S. I., M. G. Donat, B. Mueller, and L. V. Alexander, 2014: No pause in the increase of hot temperature extremes. *Nat. Clim. Change*, **4**, 161–163.

Shaman, J., S. K. Esbensen, and E. D. Maloney, 2009: The Dynamics of the ENSO–Atlantic Hurricane Teleconnection: ENSO-Related Changes to the North African–Asian Jet Affect Atlantic Basin Tropical Cyclogenesis. *J. Clim.*, **22**(9), 2458–2482.

Sillmann, J. and M. Croci-Maspoli, 2009: Present and future atmospheric blocking and its impact on European mean and extreme climate. *Geophys. Res. Lett.*, **36**(10), 92–103.

Smeed, D. A., G. McCarthy, S. A. Cunningham, E. Frajka-Williams, D. Rayner, W. E. Johns, C. S. Meinen, M. O. Baringer, B. I. Moat, A. Duchez, and H. L. Bryden,

Accepted for publication in *Journal of Climate*. DOI10.1175/JCLI-D-19-0536.1.

2014: Observed decline of the Atlantic meridional overturning circulation 2004-2012. *Ocean Sci.*, **10**, 29–38.

Steinman, B., M. Mann, and S. K. Miller, 2015: Atlantic and Pacific multidecadal oscillations and Northern Hemisphere temperatures. *Science*, **347**, 988–989.

Stadtherr, L., D. Coumou, V. Petoukhov, S. Petri, and S. Rahmstorf, 2016: Record Balkan floods of 2014 linked to planetary wave resonance. *Sci. Adv.*, **2**, e1501428.

Strong, C. and R. E. Davis, 2008. Variability in the position and strength of winter jet stream cores related to northern hemisphere teleconnections. *J. Clim.*, **21**, 584–592.

Stott, P. A., D. A. Stone, and M. R. Allen, 2004: Human contribution to the European heatwave of 2003. *Nature*, **432**(7017), 610–614.

Sun, J. 2014. Record-breaking SST over mid-North Atlantic and extreme high temperature over the Jianghuai–Jiangnan region of China in 2013. *Chinese Science Bulletin*, **59**(27), 3465–3470.

Accepted for publication in *Journal of Climate*. DOI10.1175/JCLI-D-19-0536.1.

Sun, C., J. P. Li, and S. Zhao, 2015: Remote influence of Atlantic multidecadal variability on Siberian warm season precipitation. *Sci. Rep*., **5**, 16853, https://doi.org/10.1038/ srep16853.

Sutton, R. T. and D. L. R. Hodson, 2005: Atlantic Ocean forcing of North American and European summer climate. *Science*, **309**, 115–118.

Sutton, R. T. and B. Dong, 2012: Atlantic Ocean influence on a shift in European climate in the 1990s. *Nat. Geosci.*, **5**, 788–792, doi:10.1038/ngeo1595.

Trouet, V., F. Babst, and M. Meko, 2018: Recent enhanced high-summer north atlantic jet variability emerges from three-century context. *Nature Comm.,* **9**(1), DOI：10.1038/s41467-017-02699-3.

Takaya, K. and H. Nakamura, 2001: A Formulation of a Phase-Independent Wave-Activity Flux for Stationary and Migratory Quasigeostrophic Eddies on a Zonally Varying Basic Flow. *J. Atmos. Sci.,* **58**(6), 608–627.

Ulbrich, U. and M. Christoph, 1999: A shift in the NAO and increasing storm track activity over Europe due to anthropogenic greenhouse Gas. *Clim. Dyn.,* **15**(7), 551–559.

Accepted for publication in *Journal of Climate*. DOI10.1175/JCLI-D-19-0536.1.

Vries, H. D., T. Woollings, J. Anstey, R. J. Haarsma, and W. Hazeleger, 2013: Atmospheric blocking and its relation to jet changes in a future climate. *Clim. Dyn.*, **41**(9–10), 2643–2654.

Wang, S., J. Huang, Y. He, and Y. Guan, 2014: Combined effects of the Pacific decadal oscillation and El Niño-southern oscillation on global land dry-wet changes. *Sci. Rep*., **4**,6651.

Watanabe, M. and M. Kimoto, 2000: Atmosphere-ocean thermal coupling in the north atlantic: a positive feedback. Quart. J. R. Meteor. Soc., **126**(570), 3343–3369.

Woollings, T. and M. Blackburn, 2012: The North Atlantic Jet stream under climate change and its relation to the NAO and EA patterns. *J. Clim.*, **25**, 886–902.

Yan, X., R. Zhang, and T. R. Knutson, 2017: The role of Atlantic overturning circulation in the recent decline of Atlantic major hurricane frequency. *Nat. Comm.*, **8**, 1695.

Zhang, J. and R. Zhang, 2015: On the evolution of Atlantic meridional overturning circulation (AMOC) fingerprint and implications for decadal predictability in the NA. *Geophys. Res. Lett.*, **42**, 5419–5426.

Accepted for publication in *Journal of Climate*. DOI10.1175/JCLI-D-19-0536.1.

Zhang, J., L. Li, Z. Wu and X. Li, 2015: Prolonged dry spells in recent decades over north-central china and their association with a northward shift in planetary waves. *Int. J. Climatol.*, **35**(15), 4829–4842.

Zhang, J., Z. Yang, and L. Wu, 2018: Skillful prediction of hot temperature extremes over the source region of ancient silk road. *Sci. Rep*., **8**(1), 6677.

Zhang, J., H. Chen, and Q. Zhang, 2019: Extreme drought in the recent two decades in northern China resulting from Eurasian warming. *Clim. Dyn.*, **52**, 2885–2902.

Zhang, R., R. Sutton, G. Danabasoglu, and K. Delworth, 2016: Comment on "The Atlantic Multidecadal Oscillation without a role for ocean circulation". *Science,* **352**, 1527.

Zhang, R. 2017: On the persistence and coherence of subpolar sea surface temperature and salinity anomalies associated with AMOC multidecadal variability. *Geophys. Res. Lett.*, **44**, 7865–7875.

Zhang, W., Z. Wang, M. F. Stuecker, A. Turner, F. F. Jin, and X. Geng, 2019: Impact of ENSO longitudinal position on teleconnections to the NAO. *Clim. Dyn.*, **52**, 257–274.

Accepted for publication in *Journal of Climate*. DOI10.1175/JCLI-D-19-0536.1.

Figure captions

Fig.1. The frequency of extreme flood (blue bar, PDSI>=3) and extreme drought (yellow bar, PDSI<=-3) in JA and the trend (red line) and 21-yr moving average filter (blue line) of total flood and drought frequency in 300 grids in western Europe (a), eastern Europe (b), central Asia (c), East Asia (d), central Russian (e) and eastern Russia (f). Blue dots mark the extremes with frequency after 2000 higher than mean value (dot line). r is tendency correlation, r_d is correlation of 21-yr moving average filter, * and ** mark 90% and 95% confidence levels from Monte Carlo test.

Fig. 2. Yearly time series of 5a moving average of 5-8 wave amplitudes(A) in JA over the 37.5°N -57.5°N latitudinal belt (a) and low-frequency wave index reflecting Silk Road pattern (b, SRP), and 5-a moving averages of AMO, NAMV and AMOC (a, b), the correlation coefficients r of amplitude and SRP index with AMO, NAMV and AMOC are from original series. Blue dots indicate the selected extratropical extremes over Eurasian continent in JA, * and ** are the same as Fig.1.

Accepted for publication in *Journal of Climate*. DOI10.1175/JCLI-D-19-0536.1.

Fig. 3. Mutation test of AMO (the first row), NAMV (the second row), AMOC (the third row), SRP (the fourth row) and A (the fifth row), UF and UB (red and blue thick lines) are variation series of positive and inverse sequence calculation, thin dot lines are 95% confidence level, black dash lines are abrupt points, red dash lines are 95% significant level of abrupt points.

Fig. 4. Difference of 200-hPa zonal wind (a, dU, shaded, unit: ms^{-1}) and wave activity flux (a, TNF, unit: m^2s^{-2}), 500-hPa geopotential height with an interval of 5 gpm (b, contours, ±dZ, unit: gpm) and surface temperature in JA (b, dTs, shaded, unit: ℃) between 2001-2018 and climatology (1979-2018). The figure also shows the climatological geopotential height, the contours of 5560-5680 gpm with an interval of 60 gpm (b, Z5560-5680, green lines), climatological jets with U=15, 20, 25, 30 ms^{-1} (a, U15-30, black lines), and jet with U=20 ms^{-1} after 2001 (a, U20-2000s, red line). Climatological jet lines are the same as below. Dots are t-test at 90% confidence level.

Accepted for publication in *Journal of Climate*. DOI10.1175/JCLI-D-19-0536.1.

Fig. 5. The first leading EOF mode of 200-hPa U wind in JA (a, shaded) and climatological jets (a, black lines), the 5a moving average of U/PC1, NAO, amplitude(A) and SRP (b); and the correlation coefficients between them. Climatological jets are the same as Fig.4. *, ** and blue dots are the same as Fig.2.

Fig. 6. LSTC index and the trend in July and August (a), the 5a moving average of JA LSTC, amplitude and SRP, and the correlation between them (b), and the regression of the 500-hPa temperature anomaly (c, dT, shaded) and geopotential height anomaly (c, dZ, black and gray contours representing positive and negative anomalies, with an interval of 5 gpm) to JA LSTC index. The averaged geopotential height contours before and after 2001 are the same as Fig. 4. * and ** are the same as Fig.2. Dots are 95% confidence level from Monte Carlo test.

Fig. 7. Regression maps of the 200-hPa wave activity flux (TNF, arrow, unit: m^2s^{-2}) to U/PC1 (a), –NAO (b), and LSTC (c) at the 90% confidence level. Climatological jets

Accepted for publication in *Journal of Climate*. DOI 10.1175/JCLI-D-19-0536.1.

(black lines) and the climatological geopotential height contours of 5560-5680 gpm (green lines) are the same as Fig.4. The TNF without 90% confidence level is masked.

Fig. 8. Barotropic energy at 300hPa after 2001(a, CK, shaded, unit: m^2s^{-2}) and baroclinic energy at 700hPa after 2001 (b, CP, shaded, unit: m^2s^{-2}) and the correlations between CK and U/PC1(c) and the correlations between CP and –NAO (d), black dots indicate 95% confidence level from Monte Carlo test.

Fig. 9. The first EOF mode of NA-SST in JA (a) and PC1(b), the time series of NAMV, AMO and AMOC (b), and the regression maps of the 200-hPa U wind (c, unit: ms^{-1}), geopotential height (d, lines, unit: gpm) and surface temperature (d, shaded, unit:℃) to the SST/PC1. Red lines in (d) are positive, and blue lines are negative. Climatological jets (black lines) in (a and c) are the same as Fig. 4a; black dots are the same as Fig.6.

Accepted for publication in *Journal of Climate*. DOI10.1175/JCLI-D-19-0536.1.

Fig. 10. Simulation geopotential height (shaded, gpm) and wind velocity (UV, arrows) at 500-hPa (a) and 200-hPa (b) with diabatic heating forcing over Europe (center: 50°N, 20°E) at 700 hPa, and geopotential height (shaded, gpm) and wind velocity (UV, arrows) at 500-hPa (c) and 200-hPa (d) with vorticity forcing. Climatological (U-clim=20, green lines) and simulated (U-sens=20, pink lines) 20-ms^{-1} U winds at 200 hPa are shown in (b, d), climatological (green lines) and simulated geopotential height (5560, 5620 and 5680 gpm, pink lines) at 500 hPa are shown in (a, c).

Fig. 11. Simulated anomalies of positive SST-mode (Sen.-Ctrl, Sensitivity minus Control) of 200-hPa U (a, shaded, unit: ms^{-1}) and TNF (a, vector, unit: m^2s^{-2}), 500-hPa geopotential height (b, shaded, unit: gpm) and UV wind velocity (b, velocity, unit: ms^{-1}) and 700-hPa air temperature (c, unit: ℃) from CESM. Climatological geopotential height (blue lines, b-c) and jet (thin black lines) are the same as Fig.4, but for the control simulation. Dots are the same as Fig.4.

Accepted for publication in *Journal of Climate*. DOI10.1175/JCLI-D-19-0536.1.

Fig. 12. Contrast of V-wind EOF mode representing sensitivity SRP (a, Sen. color shaded) and climatological SRP (a, lines) and the central pathway (red/ blue is Sen. and Ctrl SPR, respectively), simulated amplitude difference (b, A Diff., green line, standardized) between 20-yr sensitivity and control simulation, and SRP low-frequency wave intensities (V/PC1) from the 20-yr control simulation (b, Ctrl Diff. blue bar) and sensitivity simulation (b, Sen. Diff. yellow bar). P-Clim and N-Clim in (a) are the positive and negative V-wind distribution.

Fig. 13. Schematic diagram summarizing three physical processes of the intensified NAMV effect on low-frequency waves (LFW) and magnification of the amplitude of quasi-stationary waves (QSW). JS: NA jet, KE: seasonal kinetic energy, energy conversion from jet to KE reflects barotropic energy; B: baroclinic energy conversion to seasonal KE; LSTC: temperature contrast between the land and sea described by $\frac{\partial T'}{\partial \lambda}$, the longitudinal temperature gradient; V', meridional wind anomaly.

Accepted for publication in *Journal of Climate*. DOI10.1175/JCLI-D-19-0536.1.

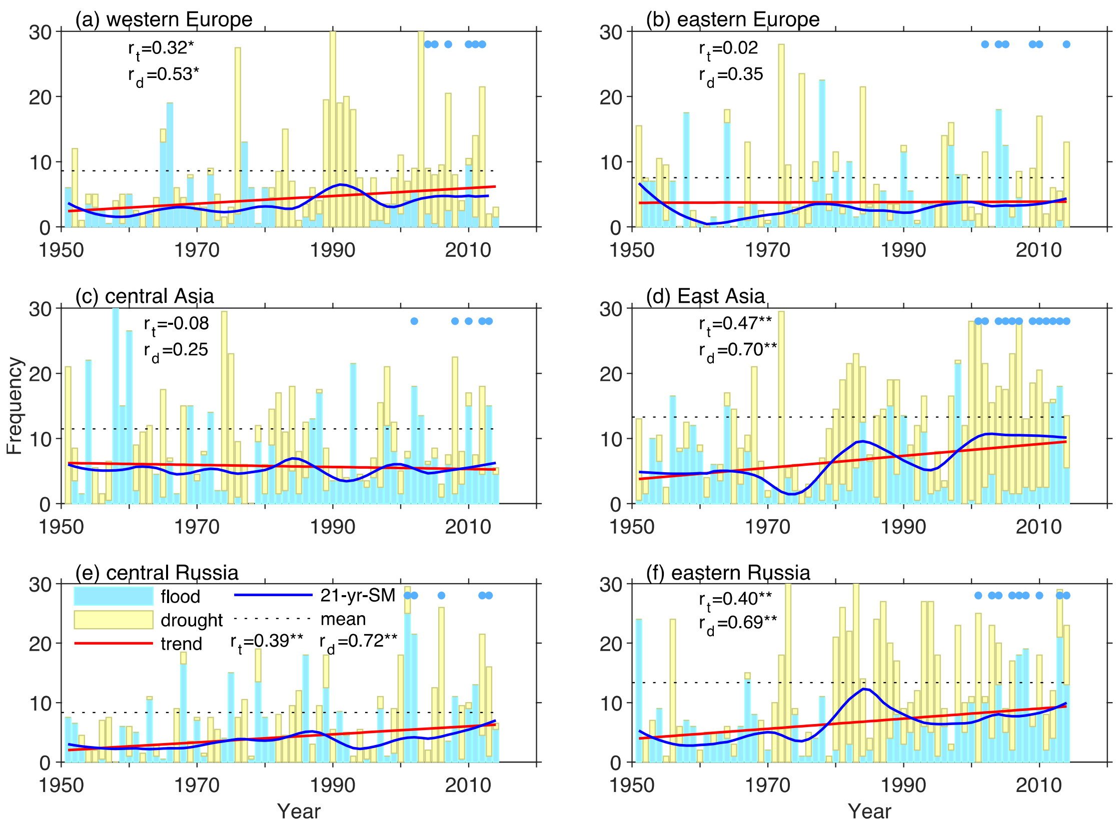

Fig.1. The frequency of extreme flood (blue bar, PDSI>=3) and extreme drought (yellow bar, PDSI<=-3) in JA, the trend (red line) and 21-yr moving average filter (blue line) of total flood and drought frequency in 300 grids in western Europe (a), eastern Europe (b), central Asia (c), East Asia (d), central Russian (e) and eastern Russia (f). Blue dots mark the extremes with frequency after 2000 higher than mean value (dot line). r is tendency correlation, r_d is correlation of 21-yr moving average filter, * and ** mark 90% and 95% confidence levels from Monte Carlo test.

Accepted for publication in *Journal of Climate*. DOI10.1175/JCLI-D-19-0536.1.

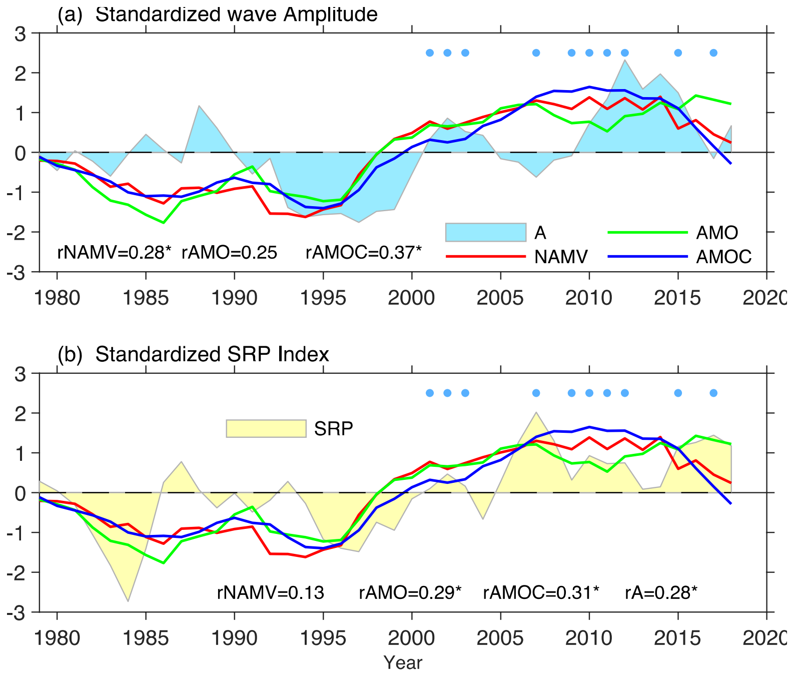

Fig. 2. Yearly time series of 5a moving average of 5-8 wave amplitudes(A) in JA over the 37.5°N -57.5°N latitudinal belt (a) and low-frequency wave index reflecting Silk Road pattern (b, SRP), and 5-a moving averages of AMO, NAMV and AMOC (a, b), the correlation coefficients r of amplitude and SRP index with AMO, NAMV and AMOC are from original series. Blue dots indicate the selected extratropical extremes over Eurasian continent in JA, * and ** are the same as Fig.1.

Accepted for publication in *Journal of Climate*. DOI10.1175/JCLI-D-19-0536.1.

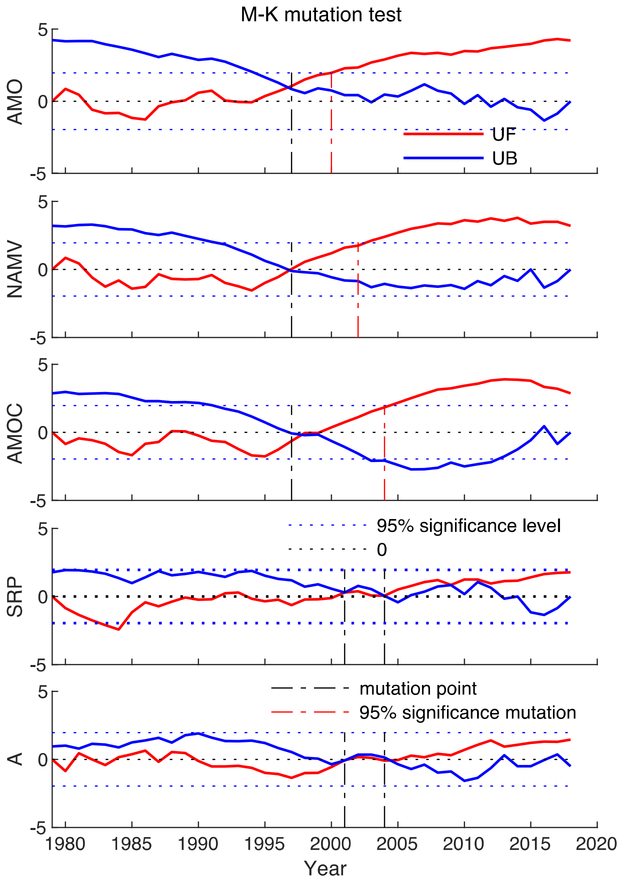

Fig. 3. Mutation test of AMO (the first row), NAMV (the second row), AMOC (the third row), SRP (the fourth row) and A (the fifth row), UF and UB (red and blue thick lines) are variation series of positive and inverse sequence calculation, thin dot lines are 95% confidence level, black dash lines are abrupt points, red dash lines are 95% significant level of abrupt points.

Accepted for publication in *Journal of Climate*. DOI10.1175/JCLI-D-19-0536.1.

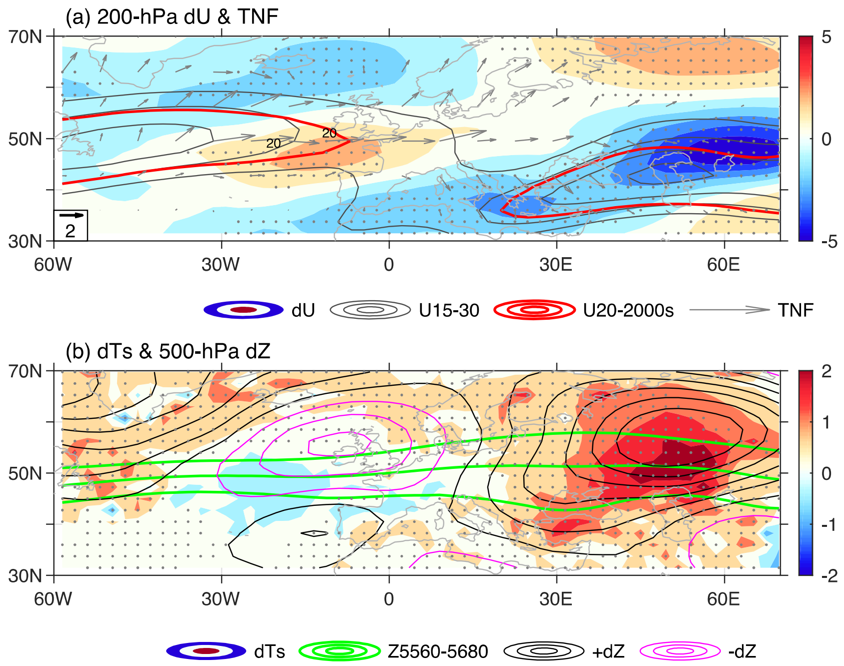

Fig. 4. Difference of 200-hPa zonal wind (a, dU, shaded, unit: ms^{-1}) and wave activity flux (a, TNF, unit: m^{2}s^{-2}), 500-hPa geopotential height with an interval of 5 gpm (b, contours, ±dZ, unit: gpm) and surface temperature in JA (b, dTs, shaded, unit: ℃) between 2001-2018 and climatology (1979-2018). The figure also shows the climatological geopotential height, the contours of 5560-5680 gpm with an interval of 60 gpm (b, Z5560-5680, green lines), climatological jets with U=15, 20, 25, 30 ms^{-1} (a, U15-30, black lines), and jet with U=20 ms^{-1} after 2001 (a, U20-2000s, red line). Climatological jet lines are the same as below. Dots are t-test at 90% confidence level.

Accepted for publication in *Journal of Climate*. DOI10.1175/JCLI-D-19-0536.1.

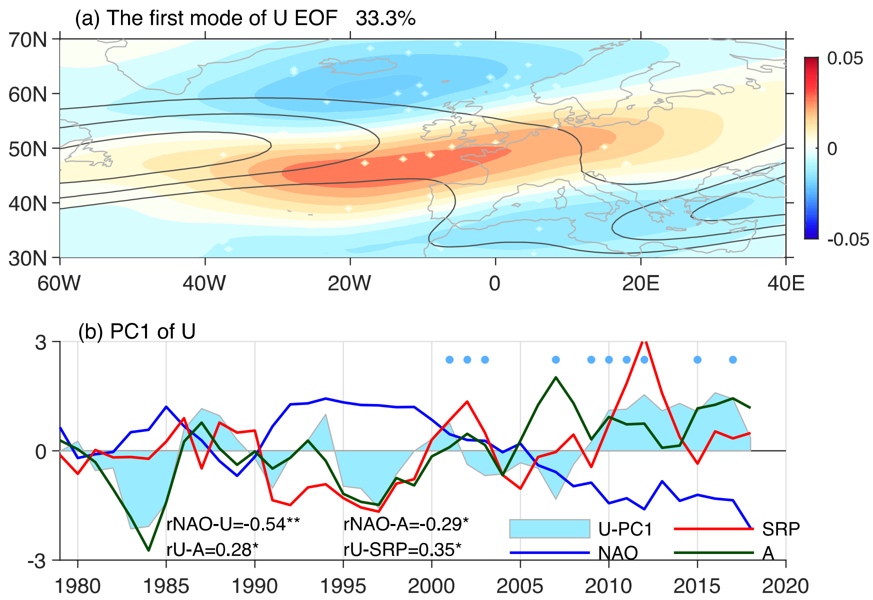

Fig. 5. The first leading EOF mode of 200-hPa U wind in JA (a, shaded) and climatological jets (a, black lines), the 5a moving average of U/PC1, NAO, amplitude(A) and SRP (b); and the correlation coefficients between them. Climatological jets are the same as Fig.4. *, ** and blue dots are the same as Fig.2.

Accepted for publication in *Journal of Climate*. DOI10.1175/JCLI-D-19-0536.1.

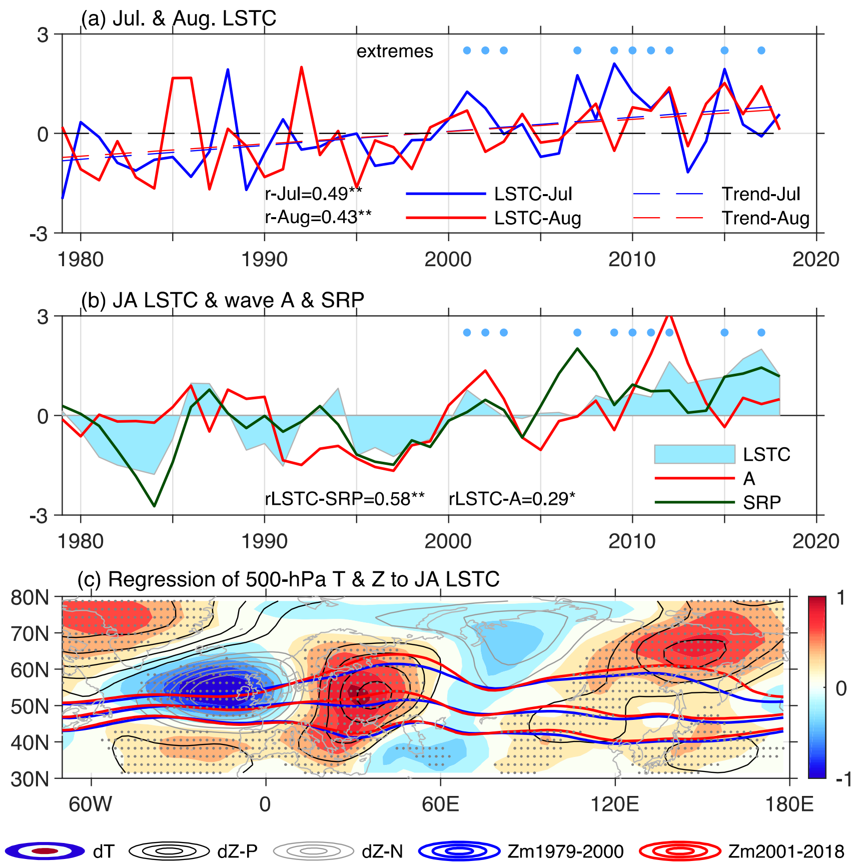

Fig. 6. LSTC index and the trend in July and August (a), the 5a moving average of JA LSTC, amplitude and SRP, and the correlation between them (b), and the regression of the 500-hPa temperature anomaly (c, dT, shaded) and geopotential height anomaly (c, dZ, black and gray contours representing positive and negative anomalies, with an interval of 5 gpm) to JA LSTC index. The averaged geopotential height contours before and after 2001 are the same as Fig. 4. * and ** are the same as Fig.2. Dots are 95% confidence level from Monte Carlo test.

Accepted for publication in *Journal of Climate*. DOI10.1175/JCLI-D-19-0536.1.

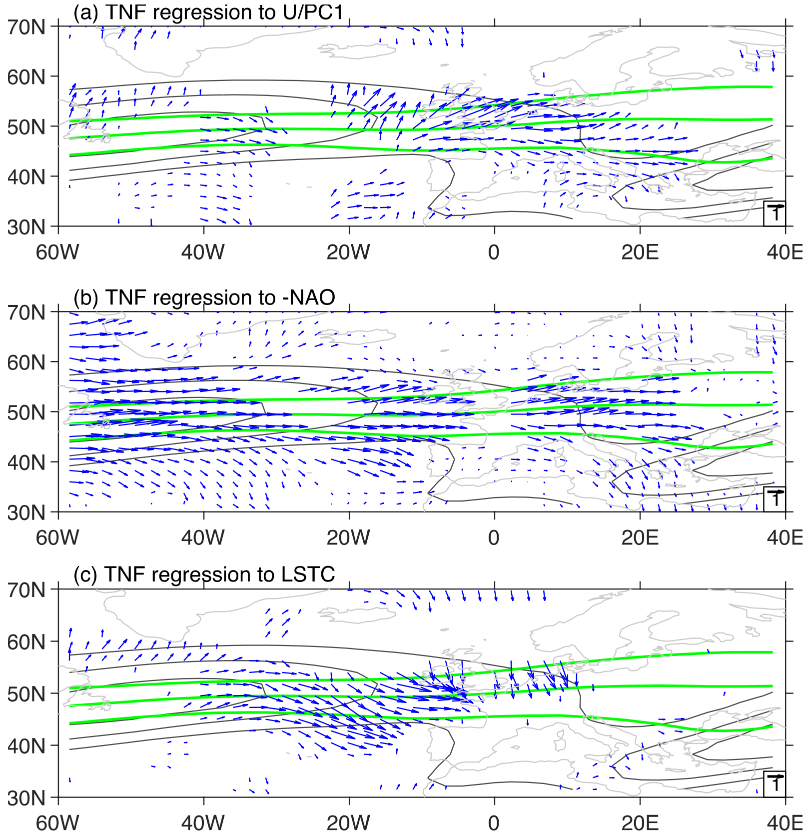

Fig. 7. Regression maps of the 200-hPa wave activity flux (TNF, arrow, unit: m^2s^{-2}) to U/PC1 (a), –NAO (b), and LSTC (c) at the 90% confidence level. Climatological jets (black lines) and the climatological geopotential height contours of 5560-5680 gpm (green lines) are the same as Fig.4. The TNF without 90% confidence level is masked.

Accepted for publication in *Journal of Climate*. DOI10.1175/JCLI-D-19-0536.1.

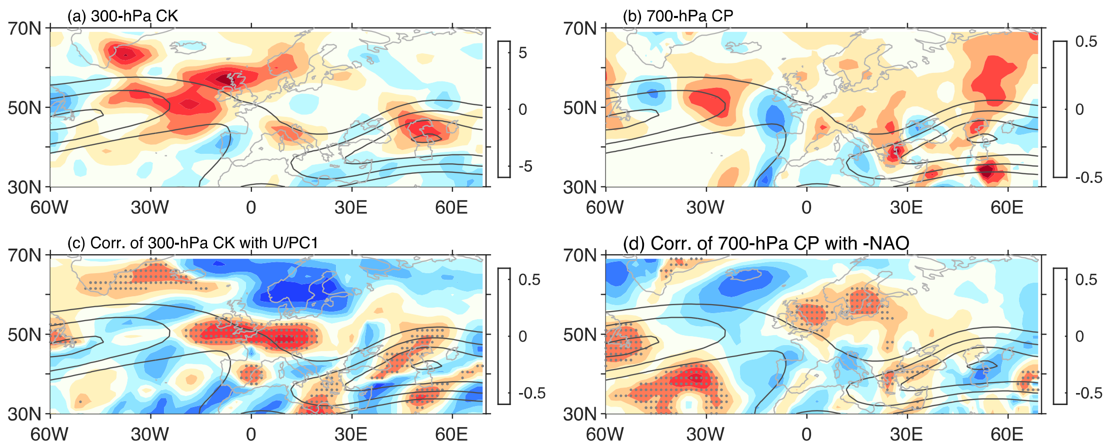

Fig. 8. Barotropic energy at 300hPa after 2001(a, CK, shaded, unit: m^2s^{-2}) and baroclinic energy at 700hPa after 2001 (b, CP, shaded, unit: m^2s^{-2}) and the correlations between CK and U/PC1(c) and the correlations between CP and –NAO (d), black dots indicate 95% confidence level from Monte Carlo test.

Accepted for publication in *Journal of Climate*. DOI10.1175/JCLI-D-19-0536.1.

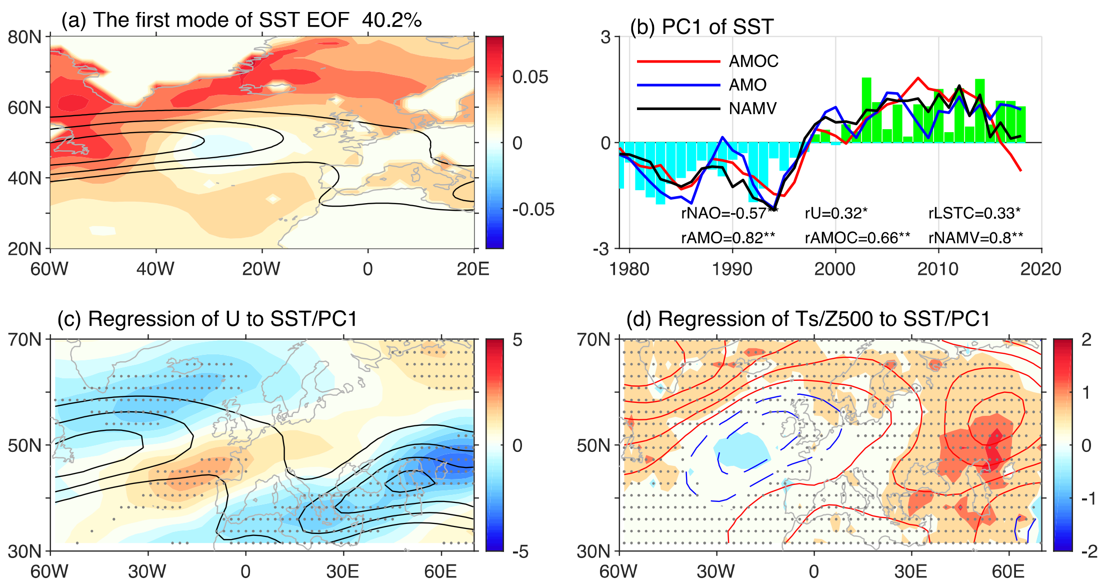

Fig. 9. The first EOF mode of NA-SST in JA (a) and PC1(b), the time series of NAMV, AMO and AMOC (b), and the regression maps of the 200-hPa U wind (c, unit: ms^{-1}), geopotential height (d, lines, unit: gpm) and surface temperature (d, shaded, unit:℃) to the SST/PC1. Red lines in (d) are positive, and blue lines are negative. Climatological jets (black lines) in (a and c) are the same as Fig. 4a; black dots are the same as Fig.6.

Accepted for publication in *Journal of Climate*. DOI 10.1175/JCLI-D-19-0536.1.

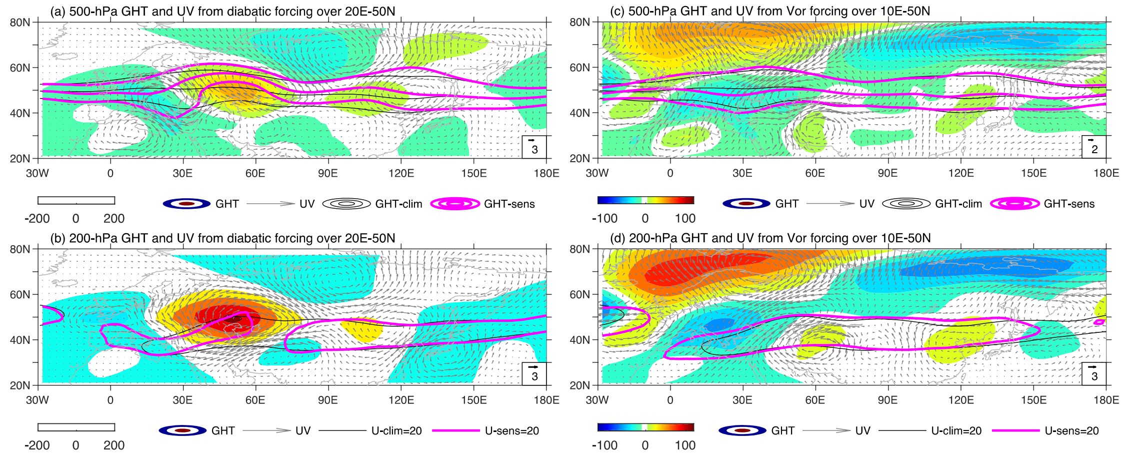

Fig. 10. Simulation geopotential height (shaded, gpm) and wind velocity (UV, arrows) at 500-hPa (a) and 200-hPa (b) with diabatic heating forcing over Europe (center: 50°N, 20°E) at 700 hPa, and geopotential height (shaded, gpm) and wind velocity (UV, arrows) at 500-hPa (c) and 200-hPa (d) with vorticity forcing. Climatological (U-clim=20, green lines) and simulated (U-sens=20, pink lines) 20-ms^{-1} U winds at 200 hPa are shown in (b, d), climatological (green lines) and simulated geopotential height (5560, 5620 and 5680 gpm, pink lines) at 500 hPa are shown in (a, c).

Accepted for publication in *Journal of Climate*. DOI 10.1175/JCLI-D-19-0536.1.

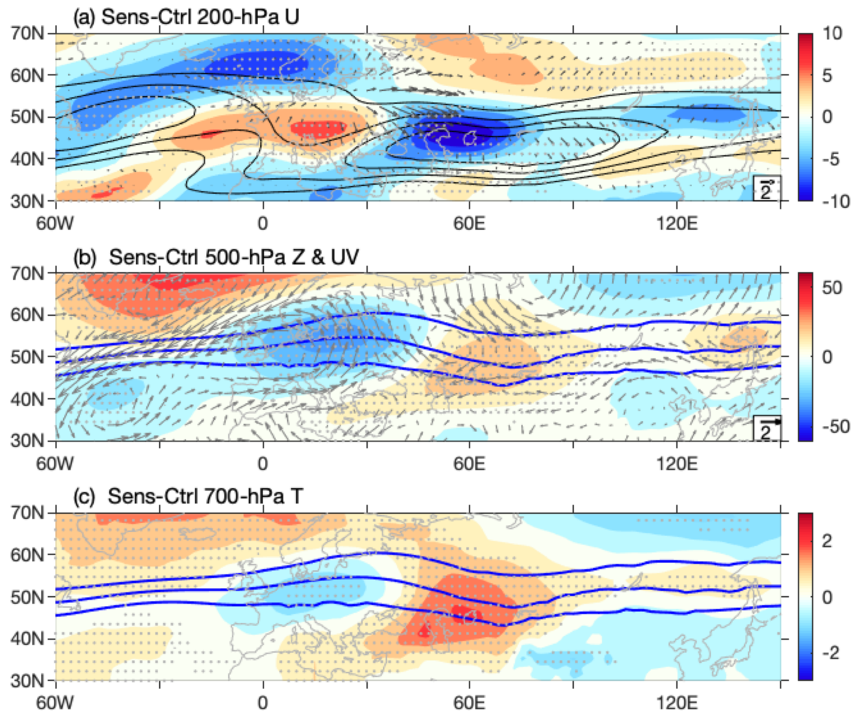

Fig. 11. Simulated anomalies of positive SST-mode (Sen.-Ctrl, Sensitivity minus Control) of 200-hPa U (a, shaded, unit: ms^{-1}) and TNF (a, vector, unit: m^2s^{-2}), 500-hPa geopotential height (b, shaded, unit: gpm) and UV wind velocity (b, velocity, unit: ms^{-1}) and 700-hPa air temperature (c, unit: ℃) from CESM. Climatological geopotential height (blue lines, b-c) and jet (thin black lines) are the same as Fig.4, but for the control simulation. Dots are the same as Fig.4.

Accepted for publication in *Journal of Climate*. DOI10.1175/JCLI-D-19-0536.1.

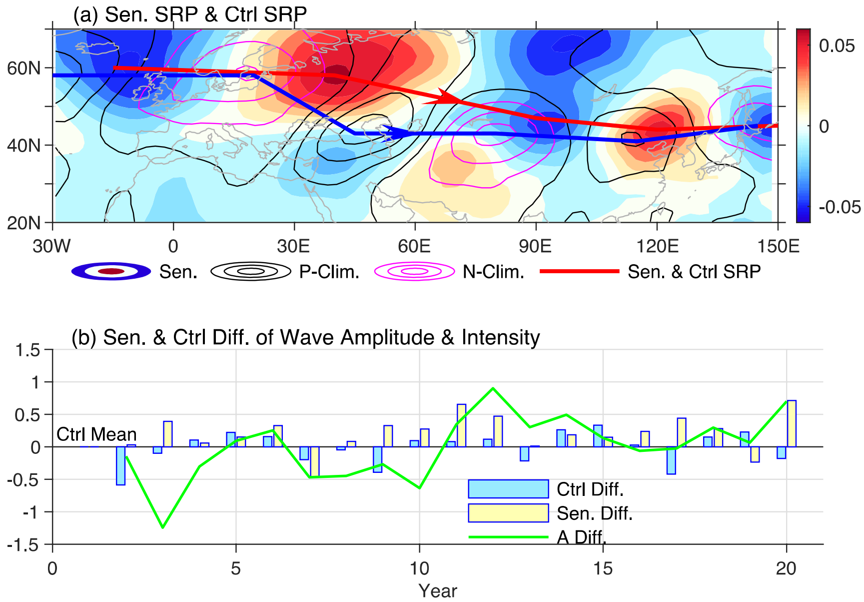

Fig. 12. Contrast of V-wind EOF mode representing sensitivity SRP (a, Sen. color shaded) and climatological SRP (a, lines) and the central pathway (red/ blue is Sen. and Ctrl SPR, respectively), simulated amplitude difference (b, A Diff., green line, standardized) between 20-yr sensitivity and control simulation, and SRP low-frequency wave intensities (V/PC1) from the 20-yr control simulation (b, Ctrl Diff. blue bar) and sensitivity simulation (b, Sen. Diff. yellow bar). P-Clim and N-Clim in (a) are the positive and negative V-wind distribution.

Accepted for publication in *Journal of Climate*. DOI10.1175/JCLI-D-19-0536.1.

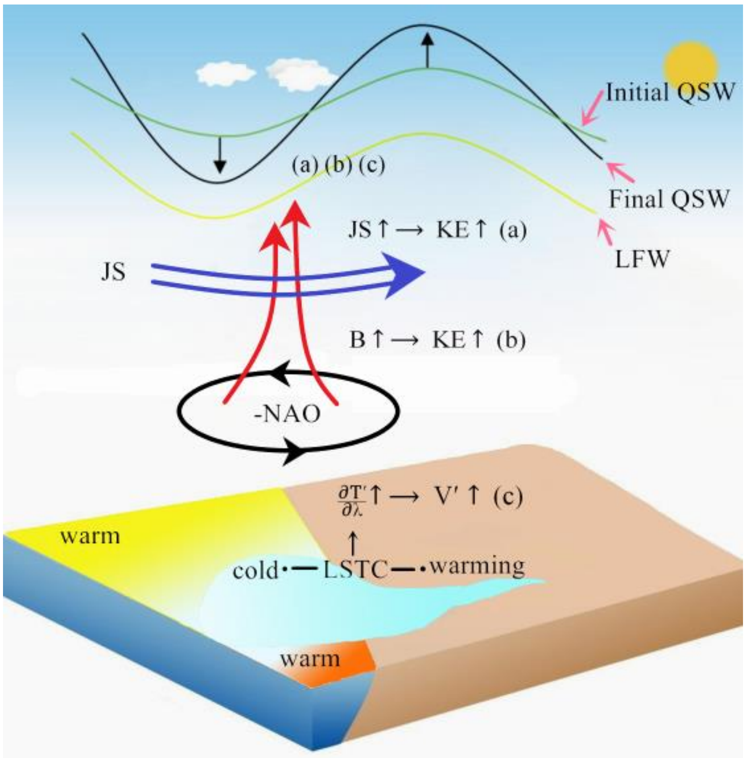

Fig. 13. Schematic diagram summarizing three physical processes of the intensified NAMV effect on low-frequency waves (LFW) and magnification of the amplitude of quasi-stationary waves (QSW). JS: NA jet, KE: seasonal kinetic energy, energy conversion from jet to KE reflects barotropic energy; B: baroclinic energy conversion to seasonal KE; LSTC: temperature contrast between the land and sea described by $\frac{\partial T'}{\partial \lambda}$, the longitudinal temperature gradient; V', meridional wind anomaly.

Accepted for publication in *Journal of Climate*. DOI 10.1175/JCLI-D-19-0536.1.